Abstract of "Thermodynamics and kinetics of strain-induced self-assembly on crystal surfaces" by Nikhil Medhekar, Ph.D., Brown University, May, 2009.

An appealing approach to manufacturing future generation nanoscale devices envisioned for electronic, magnetic and photonic applications is to exploit the natural tendency of small material clusters to self-organize into well-defined patterns. While strain-driven self-assembly is widely viewed as a promising technique for patterning at the nanoscale, to follow this approach and create structures in a desired manner, a reliable means to engineer the characteristic size and shapes that the clusters adopt during self-assembly is essential. Motivated by a significant potential technological impact, a systematic elucidation of how long-range elastic interactions couple with surface and bulk thermodynamics and kinetics to control shape, size and compositional patterns assumes a paramount importance. The work presented here describes a detailed analysis of evolution of morphological and compositional patterns in various strain-driven self-assembled systems. The examples include alloy quantum dots and 2D patterns such as surface stress domains and epitaxial nanowires. Using a combination of experimental, numerical and analytical techniques, it is shown that the elastic strain inherent in these systems leads to dramatic transformations the compositional and morphological patterns that are not predicted by existing theoretical models. Many of these systems can remain trapped in a large variety of long-lived and metastable shapes that arise from an interplay of crystalline anisotropy and relaxation of elastic strain. Based on experimental observations coupled with dynamic growth simulations, we have developed a quantitative understanding of how a self-assembling system falls out of equilibrium. Further, using a combination of finite element and optimization methods, a systematic description of the interplay between the composition variations, temperature, strain and the morphology is developed.

Thermodynamics and kinetics of strain-induced self-assembly on crystal surfaces

by

Nikhil Medhekar

Sc. M., Applied Mathematics, Brown University, 2006

M. Tech., Mechanical Engineering, Indian Institute of Technology, Bombay, 2002

Bachelor of Engineering, Mechanical Engineering, University of Pune, 2000

A dissertation submitted in partial fulfillment of the
requirements for the Degree of Doctor of Philosophy
in the Division of Engineering at Brown University

Providence, Rhode Island

May, 2009

This dissertation by Nikhil Medhekar is accepted in its present form by the Division of Engineering as satisfying the dissertation requirement for the degree of Doctor of Philosophy.

Date _____ _____

Professor Vivek B. Shenoy, Advisor

Recommended to the Graduate Council

Date _____ _____

Professor L. Ben Freund, Reader

Date _____ _____

Professor Eric Chason, Reader

Approved by the Graduate Council

Date _____ _____

Professor Sheila Bonde
Dean of the Graduate School

Vita

Nikhil Medhekar was born on January 1, 1979 in Yeola, district Nashik, India. He studied up to the tenth grade at Nutan Marathi Vidyalay High School in Pune and spent the next two years at Sir Parshurambhau Junior College, Pune. He then joined the College of Engineering, Pune in 1996 for his Bachelor's degree in Mechanical Engineering. Afterwards, he continued his studies in Mechanical Engineering at the Indian Institute of Technology, Mumbai (known as Bombay at that time) for Master's degree in Mechanical Engineering. After graduating from the Indian Institute of Technology in January 2002, Nikhil worked in the Advanced Mechanical Technologies group at the General Electric research center in Bangalore, India. Nikhil joined the Solid Mechanics program at Brown University in the Fall of 2003. En route to his Ph.D., he received a Masters degree from Brown in Applied Mathematics in 2006. He plans to pursue postdoctoral research at the Brown University after his Ph.D. with the eventual aim of a career in acadmia.

Acknowledgements

I am profoundly grateful to my thesis supervisor, Professor Vivek Shenoy. His joy of discovery, his infectious enthusiasm and his sustained encouragement have made these past few years at Brown highly rewarding. I would like to express my gratitude to my readers Professor Freund and Professor Chason for taking time out of their schedules to review and critique my work. I have taken the opportunity several times over the past few years to knock on Professor Freund's door with a multitude of questions – academic or otherwise – and he has always been kind enough to indulge me.

My thanks are due to my colleagues, past and present, who have contributed to making my academic life at Brown stimulating. At the risk of offending those inadvertently left out, I would like to mention Ashwin Ramasubramaniam, Dhananjay Tambe, Eric Buchovecky, Ramanarayan Hariharputran, Prateek Nath, Vinay Gill, Julie Waters, Wai Lun Chan, Srikanth Srigiriraju, Narendra Singh, Jean Gullickson, Donald Ward, Shumann Xia, Andrea Cavicchi, Ningning Du, Tanmay Bhandakkar, Rassin Grantab, Brian Burke, Steve Grunchel, Asha Nurse, Badiruzzaman Syed, Dhiraj Catoor and Vishwanath Hegadekatte. I would also like to express my gratitude to Olga Koshevaya, Anuradha Bhat, Laruren Wier, Paulo Guilhardy, Sangeeta Choudhari, Bharathi, Shehnaz Warsi, Rashmi Padiappu, Patra Jongjitirat, LeAnne Edwards, Jacob Basel and members of Brown Ballroom Dance Team for being the source of much happiness in my non-academic life.

No acknowledgment could possibly be complete without thanking my parents and siblings for their affection and support throughout my endeavors.

Contents

⋆ Parts of this thesis have appeared in the following peer-reviewed publications:

Medhekar, N. V., Shenoy, V. B., Hannon, J. B. and Tromp, R. M. (2007), 'Metastability in 2D self-assembling systems', *Physical Review Letters* **99** (156102).

Medhekar, N. V., Shenoy, V. B., Hannon, J. B. and Tromp, R. M. (2007), 'Self-assembling surface stress domains far from equilibrium', *Applied Physics Letters* **91** (253101).

Medhekar, N. V. and Shenoy V. B. (2008), 'Shape dynamics in anisotropically strained 2D self-assembling systems', *Journal of Applied Physics* **103** (063523).

Medhekar, N. V., Hegadekatte, V. and Shenoy, V. B. (2008), 'Composition maps in self-assembled alloy quantum dots', *Physical Review Letters* **100** (106104).

List of Tables

List of Figures

Chapter 1

Introduction and overview

As the trend goes, future generation computer and electronic systems will require higher speed, lower power consumption and reduced size. However, the advantages of further miniaturization of integrated circuits reach beyond increasing the device density of a chip. When device dimensions become comparable to characteristic lengths such as the electronic wavelength or magnetic domain width, electron-localization and size effects can lead to new quantum mechanical phenomena such as Peierls transition and Luttinger liquid behavior [Datta (2005)]. New generation of electronic, photonic, and magnetic devices built from these miniaturized structures are expected to form the functional elements or building blocks for technologies based on quantum computing and molecular electronics. To realize these new technologies, the sizes of the devices usually need to be in the single-digit-nanometer scale or even less. Historically, the semiconductor industry has been able to meet the increasing demand for miniaturization by doubling chip density every 18 months, due in large part to significant advances in lithographic patterning techniques [Moore (1965)]. However, the current state of the art of 40 nm features has already approached the limits of UV-light based lithography [Silverman (1998)]. To maintain the current pace of development, a fundamental shift from the conventional integrated circuit fabrication

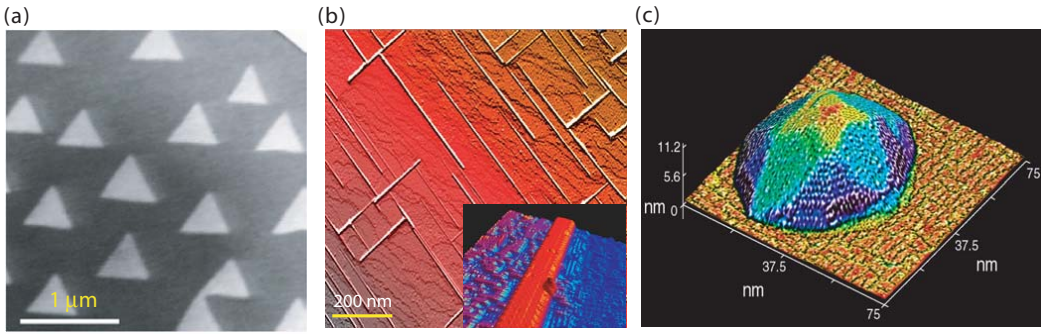

Figure 1.1: Examples of strain-induced self-assembly at the nanoscale. (a) Low energy electron microscopy images of strain-stabilized surface stress domains on Si(111) [Hannon *et al.* (2002)]. (b) Scanning Tunneling Microscopy topograph of $ErSi_2$ nanowires grown on Si(001) [Chen *et al.* (2002)]. The inset shows a typical $ErSi_2$ nanowire that is 9 atoms wide and 250 nm long. (c) Scanning Tunneling Microscopy image of a dome-shaped Ge quantum dot on Si(001) [Medeiros-Ribeiro *et al.* (1998)].

paradigms is required [Williams (2007)].

A particularly appealing approach to manufacturing nanoscale devices is to exploit the natural tendency of small material clusters to self-organize. A bottom-up or natural self-assembly approach has become the method of choice, and is being actively investigated as an alternative to the current top-down lithographic approach [Whitesides and Grzybowski (2002)]. On semiconductor surfaces, elastic interactions arising from lattice mismatch in heteroepitaxial thin films or due to differences between atomic structures can give rise to spontaneous formation of self-assembled nanoscale structures such as surface patterns [Seul and Andelman (1995), Pohl *et al.* (1999), Plass *et al.* (2001), Hannon *et al.* (2002)], epitaxial nanowires [Sunamura *et al.* (1996), Evans and Nogami (1999), Chen *et al.* (2002), You *et al.* (2006), Owen *et al.* (2006), Sone *et al.* (2007), Lim *et al.* (2007), Li *et al.* (2007)] and quantum dots [Medeiros-Ribeiro *et al.* (1998), Ross *et al.* (1999), Drucker (2002), Stangl *et al.* (2004)]. As an example, some of the self-assembled structures are shown in Fig. 1.1. The nanoscale 2D patterns can serve as templates for growing 3D nanostructures,

while the nanowires – which can allow the use of a wide range of materials systems such as Ga, Bi, CaF_2 and Pt, Dy and Ho silicides – can be potentially employed as interconnects in the integrated circuits. Self assembled SiGe [Fig. 1.1(c)] and InGaAs quantum dots have received wide attention as the former material system can be readily integrated with the well developed Si integrated circuit technology [Drucker (2002), Singh *et al.* (2005)] while the latter has been successfully applied in photovoltaic and photonic bandgap applications [Bimberg *et al.* (1993)].

While strain-driven self-assembly is widely viewed as a promising technique for patterning at the nanoscale, to follow this approach and create structures in a desired manner, a reliable means to engineer the characteristic size and shapes that the nanostructures adopt during self-assembly is essential. The tremendous potential technological impact has therefore attracted a strong scientific interest in past few years in the physical processes that govern the growth of these structures. Whereas significant advances have been made regarding the surface science [Pimpinelli and Villain (1998)] and the mechanics of thin films [Freund and Suresh (2003)], an understanding of how long-range elastic interactions couple with surface and bulk thermodynamics and kinetics to control shape, size and compositional patterns remains lacking. To this end, a systematic elucidation of the interplay between thermodynamics, mechanics and kinetics of nanoscale self-assembly is of paramount importance. This essentially is the topic of this thesis in a very broad sense.

In this thesis, using a combination of experimental, numerical and analytical techniques, we have analyzed evolution of morphological and compositional patterns in various strain-driven self-assembled nanostructures. The work presented here can be broadly categorized into two subtopics: In the first subtopic (Chapters 2-4), we study morphological evolution of 2D patterns such as stress domains and epitaxial nanowires, while the second subtopic (Chapter 5) is concerned with compositional

patterns in alloy quantum dots. In Chapter 2, the role of long-range elastic interaction in far from equilibrium growth of stress domains on Si(111) is investigated using numerical phase-field calculations backed by electron microscopy experiments. Chapter 3 describes the metastability in domain shapes that gives rise to a wide variety of shapes on typical cubic (111) surfaces – the shapes that are not observed in any other material system. In Chapter 4, we show that when the strain is anisotropic, it can couple in unique ways with the growth kinetics resulting in shapes that are not predicted by existing theoretical models. Finally, as described in Chapter 5, we develop the equilibrium composition maps for strained alloy quantum dots using an efficient numerical scheme that couples finite element methods with quadratic programming optimization.

The thesis is organized in a way that the introductory parts of each chapter will provide the reader with sufficiently detailed background information and references to the literature. Therefore, any additional remarks of introductory nature are not included here.

Chapter 2

Self-assembling surface stress domains far from equilibrium

2.1 Introduction

It is well known that long-range elastic, electrostatic, or magnetic interactions can induce the spontaneous formation of 2D periodic patterns in two-phase systems [Seul and Andelman (1995)]. In many cases, the features have nanoscale dimensions, making them of interest for sub-lithographic surface templating. Theoretical studies have shown that regular and well-ordered patterns and shapes are favorable from a thermodynamic point of view as they lower the total free energy of the system. Therefore, patterning can be easily achieved in systems that can be quickly equilibrated. Furthermore, their characteristic feature sizes are directly related to surface thermodynamic parameters [Alerhand *et al.* (1988), Tersoff and Tromp (1993), Li *et al.* (2000), Plass *et al.* (2001), Hannon *et al.* (2002), Thayer *et al.* (2004)], which can then be extracted from experiments in material systems that are easily equilibrated [Brongersma *et al.* (1998), van Gastel *et al.* (2006)]. While there is generally a 'down

hill' path in energy from any non-equilibrium structure towards the stable one in the absence of long-range interactions, these interactions can give rise to complex energy landscapes that make equilibration practically impossible in many material systems. Development of a quantitative understanding of how and if self-assembling systems reach and fall out of equilibrium is therefore crucial for evaluating the technological promise of spontaneous self-assembly.

In this chapter, we study the growth of isolated stress domains on Si(111) surfaces far from equilibrium using *in situ* electron microscopy. We find that the shapes of large domains (area $> 1\ \mu m^2$) are fundamentally different from those of smaller domains. While small domains always adopt compact shapes, large domains have more ramified shapes, such as the shape with serrated edges in Fig. 2.2(a) and the connected-triangle morphology in Fig. 2.2(b). Why do large domains develop multiple serrations along their edges and adopt more ramified shapes? Using dynamic growth simulations, we show that the formation of serrations, or notches, is driven by elastic relaxation. Notch formation lowers the formation energy of large domains; however, whether or not the notches appear during growth is governed by the anisotropy in the free energy of the domain boundary – large anisotropy leads to notch formation at smaller sizes, while notches may never form when the anisotropy is small. Once notches form, the domain evolves towards a ramified shape consisting of connected triangles of similar size. Since notch formation is very sensitive to the azimuthal dependence of the boundary energy, this key thermodynamic function that governs self assembly can be more reliably determined by analyzing the non-equilibrium shapes that the domains adopt as they grow in size. Similar morphologies, i. e., large domains with serrated boundaries or the domains formed by connecting small domains, are expected for a wide range of self-assembling systems with long-range interactions. Our work shows that the interplay of the anisotropy in bond energetics and strain relaxation leads to

novel transitions in growth shapes that are not observed in unstrained systems, and that are distinct from the shape transitions predicted for equilibrium shapes [Tersoff and Tromp (1993), Brongersma *et al.* (1998), Li *et al.* (2000), Thayer *et al.* (2004), van Gastel *et al.* (2006)].

The rest of the chapter is organized as follows: In Sec. 2.2, we briefly outline the thermodynamics of the surface phase transition on Si(111) and the subsequent formation of surface stress domains. Sec. 2.3 describes *in situ* microscopy observations of morphological evolution of large stress domains during growth and annealing. An analysis of a continuous transition in the equilibrium shapes of small domains is given in Sec. 2.4. In Sec. 2.5, we describe the formulation of a dynamic growth model which accounts for the thermodynamics as well as kinetics of the growth of stress domains. In Sec. 2.6, we discuss in detail the morphological evolution of stress domains, based on the dynamic growth simulations. Finally, the conclusions drawn from our analysis are summarized in Sec. 2.7.

2.2 Surface phase transition and stress domains on Si(111)

It is well known that Si(111) surface exhibits a classic first order phase transition in the surface structure. When heated above the critical temperature $T_C = 862$ °C, the surface converts from a complex (7×7) structure to a nearly-disordered (1×1) phase [Takayanagi *et al.* (1985)]. Above T_C, the (1×1) phase has a lower surface energy than the (7×7) phase, which would suggest that a (7×7) domain cannot coexist in thermodynamic equilibrium with the (1×1) surface for $T > T_C$. However, at temperatures just above T_C, the domains of the the low-temperature, reconstructed (7×7) surface phase coexist with the high-temperature (1×1) phase, as shown in

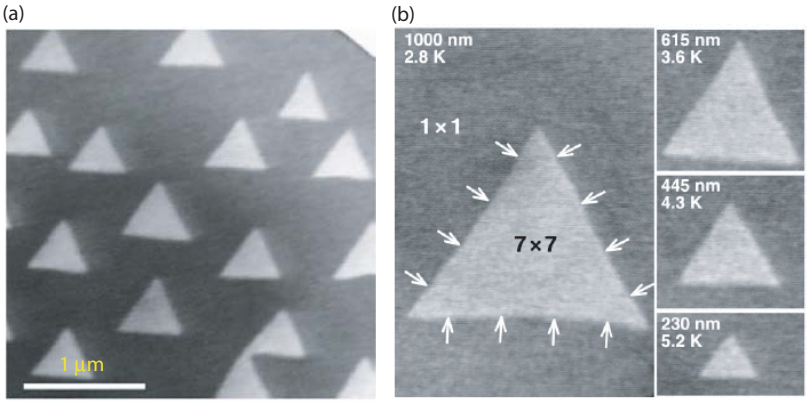

Figure 2.1: Surface stress domains on Si(111) [Hannon *et al.* (2002)]. (a) 10 eV bight-field LEEM images of self-assembled domains on Si(111). The bright areas correspond to (7×7) structures, while dark areas indicate (1×1) structures. (b) LEEM images of an isolated (7×7) domain at four temperatures above T_C. Each panel is labeled by the side length of the domain, as well as by $(T - T_C)$. Arrows indicate the orientations of force monopoles due to the difference in the surface stress in two phases. The domain shrinks as the temperature is increased, indicating that the temperature can be used as a means to control their equilibrium size.

Fig. 2.1(a).

This coexistence is attributed to the surface stress in (7×7) and (1×1) phases [Hannon *et al.* (2001)]. The surface stress in (7×7) phase is tensile while it is compressive in (1×1) phase. The difference in surface stress $\Delta\sigma = (\sigma_{7\times7} - \sigma_{1\times1})$ has been determined to be 30 meV/°A^2 [Twesten and Gibson (1994)]. Due to the long-range elastic interactions arising from the the difference in surface stress [refer Fig. 2.1(b)], formation of a (7×7) domain allows for relaxation of surface stress at the domain boundary. Phase coexistence occurs when the gain in elastic relaxation energy at the boundary offsets the cost of forming the unfavorable phase. A quantitative analysis of the competition between these two contributions to the total free energy shows that coexistence of (7×7) with (1×1) is possible as long as $(T - T_C) < 5.3$ °C [Hannon *et al.* (2002)]. The surface temperature provides a means for controlling the equilibrium size of the (7×7) domain – the size of the coexisting domain decreases continuously

as temperature is raised above T_C as depicted clearly in Fig. 2.1(b). Depending on the rate at which the temperature is varied, domains can be grown near or far from thermodynamic equilibrium. Thus, an interplay between elastic relaxation, surface free energy, and the phase boundary creation energy leads to novel and distinct phenomena: isolated (7×7) domains that are stable above T_C, and whose equilibrium size can be tuned by changing the temperature.

2.3 *Real time* in situ *microscopy observations*

In our experiments, we have used *in situ* Low-Energy Electron Microscopy (LEEM) [Tromp and Reuter (1991)] to image the Si(111) surface near the phase transition temperature, $T_C = 862$ °C. We have focused our analysis on isolated (7×7) domains on large, step-free terraces – a configuration that can be directly modeled theoretically. These experiments were performed by our collaborator Dr. James Hannon at IBM T. J. Watson Research Center.[1]

Typical domain shapes observed during the growth and annealing of large domains are shown in Fig. 2.2(a) and Fig. 2.2(b), respectively. In the sequence shown in Fig. 2.2(a), the domain grows as the temperature is lowered by 1.6 °C over an interval of 450 seconds (movie S1), while in the sequence shown in Fig. 2.2(b) the domain is grown at a very slow rate by lowering the temperature by just 0.5 °C over same time interval (movie S3). Fig. 2.2(c) shows the sequence of images when large domains with ramified shapes are annealed at fixed temperature (movie S2).

During fast growth, domain boundaries that are initially straight, gradually bend inward until two notches appear at a size of 3 μm^2 as shown in Fig. 2.2(a). As the domain grows still larger (i.e. temperature decreased further), more notches appear

[1]The real time movies of LEEM observations showing out-of-equilibrium growth and annealing of large stress domains can be down-loaded from the http://nikhil.medhekar.googlepages.com/movies

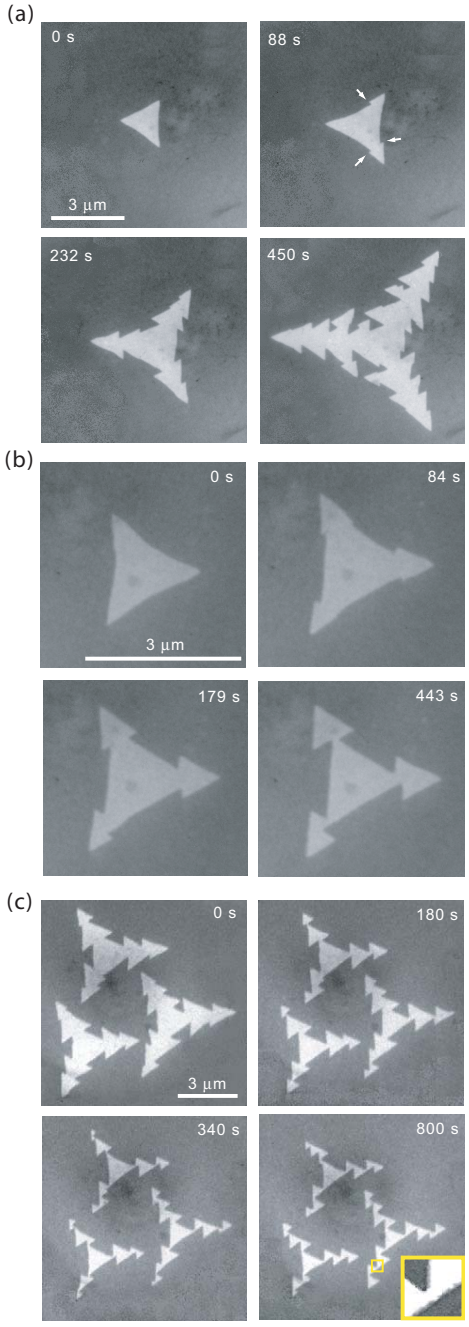

Figure 2.2: Sequence of 10 eV bight-field LEEM images of an isolated (7×7) stress domains during (a) fast growth, (b) slow growth and (c) annealing. Growth sequence in part (a) and (b) is achieved by lowering the surface temperature in the duration of 450 sec from 865.6 °C to 864.3 °C and 865.6 °C to 865.1 °C, respectively. The sequence in part (c) is obtained by annealing the surface at 864 °C for 800 seconds. The images are labeled by acquisition time in seconds.

on the boundary, resulting in a roughly triangular shape, but one with serrated sides. Domains that are grown to large size more slowly [Fig. 2.2(b)], or ones that are held at constant temperature for a long time [Fig. 2.2(c)], have qualitatively different shapes. Rather than serrated sides, these domains more closely resemble a group of connected triangular domains of similar area.

It is evident from Fig. 2.2(a) and Fig. 2.2(c) that the shapes with serrated edges are *far from equilibrium* as they eventually evolve to connected-triangle morphology when held at constant temperature. In distinct contrast, small compact domains obtained during early stages of growth do not undergo significant shape transformation when held at fixed temperature. Clearly, while the shapes of small domains can be changed in a reversible manner, large domains show significant hysteresis in their shape evolution indicating that the shape has not equilibrated.

Why are the shapes of large domains so characteristically different than the shapes of small domains? Why do large domains develop serrations along the boundaries when grown at a fast rate while slower growth leads to connected-triangle morphology? Before analyzing the details of how large domains grow out of equilibrium, we consider the evolution of equilibrium shapes of small domains in the following section.

2.4 Continuous transitions in equilibrium domain shapes

In a recent study, Thayer et al. [Thayer *et al.* (2004)] investigated the orientation-dependence of the free energy of the domain boundary by analyzing how the equilibrium shape of small domains changes with size. They found that domains smaller than 0.3 μm^2 have sides that are bent outward [i.e. convex, as seen in Fig. 2.3(a)] while the sides of larger domains were bent inward [i.e. concave, refer Fig. 2.3(c)].

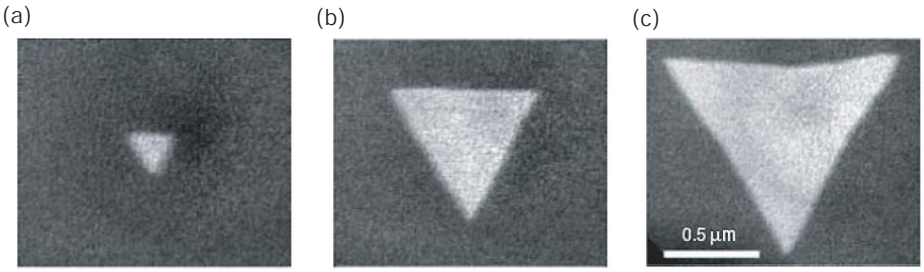

Figure 2.3: Continuous transition in the equilibrium shapes of stress domains on Si(111) [Thayer *et al.* (2004)]. LEEM images of isolated equilibrium domain shapes. As the size increases, the domain undergoes a continuous shape transition from convex to concave. The size of the domain shown in panels (a-c) are 0.01, 0.27 and 1.10 μm^2, respectively.

This magnitude of 'bend' can be characterized by defining the ratio b/L as shown in Fig. 2.4(a). By analyzing the magnitude of bend during the continuous covex to concave transition in the equilibrium domain shapes, Thayer et. al. were able to estimate the degree of anisotropy in the boundary energy [Thayer *et al.* (2004)].

Since the bend is a rather coarse characterization of the shape, it is important to see if it can be used to unambiguously determine the boundary energy. To see how sensitive the measured bend is to the anisotropy in the edge energy, we have computed the equilibrium shapes of domains for a simple parameterization of the three-fold symmetric boundary energy, $\beta(\theta) = \beta_0 + \beta_1(1 - \cos 3\theta)$, θ being the orientation of the boundary [or, the angle made by the normal to boundary with x_1 axis, refer inset in Fig. 2.4(a)]. Here β_0 is the cost of creating the boundary along low-energy directions on Si(111) surface and the parameter β_1 controls the degree of anisotropy in the boundary energy. Specifically, we minimize the total energy of a domain at constant area,

$$E = \int_s \beta(\theta)\, ds - \frac{1}{2}\Delta\sigma \int_s \mathbf{n}(s) \cdot \mathbf{u}(s)\, ds\,, \tag{2.1}$$

where the integrals are taken over the perimeter of the domain. The first term in Eq. 2.1 represents the cost of creation of domain boundary, which is now characterized

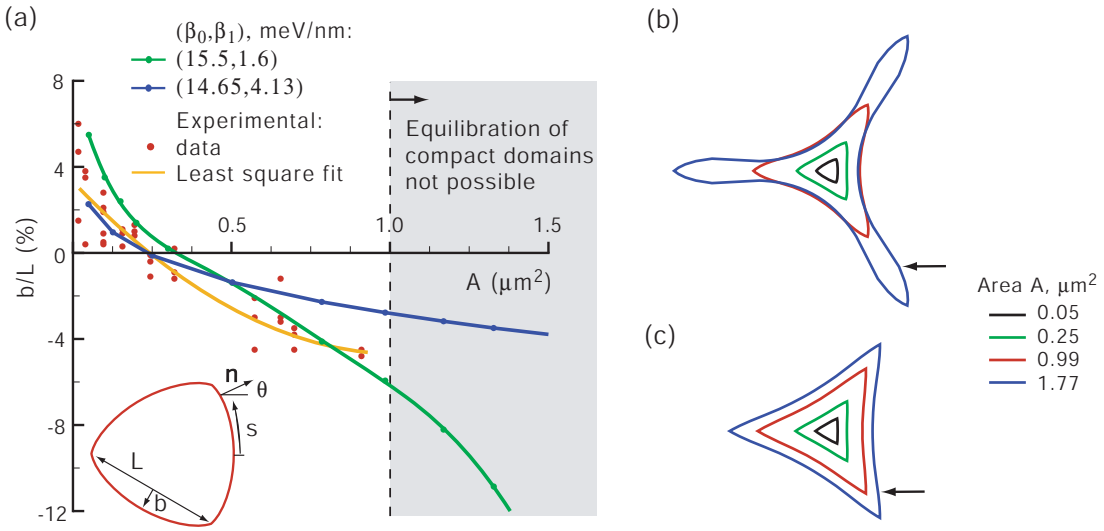

Figure 2.4: (a) Bend (b/L, where b and L are defined in the inset) in the equilibrium shapes of strained domains plotted as a function of their area, A. The red circles represent experimental measurements [Thayer *et al.* (2004)] and computed bends for the boundary energies characterized by parameters (β_0, β_1) (indicated in the figure) are given by green and blue curves. (b-c) The equilibrium shapes for the cases (β_0, β_1) = (15.5,1.6) and (14.65,4.13) meV/nm are given in (b) and (c), respectively. The arrows in the shapes corresponding to A = 1.77 μm^2 indicate the points of inflection.

by two parameters (β_0, β_1). The second term is the elastic energy due to the difference in the surface stress in the (7×7) phase and the (1×1) phase, $\Delta\sigma = (\sigma_{7\times7} - \sigma_{1\times1}) =$ 30 meV/°A^2 [Twesten and Gibson (1994)]. $\mathbf{n}(s)$ denotes the outward normal to the domain, while $\mathbf{u}(s)$ is the displacement field due to elastic relaxation. We have used isotropic linear elastic Green's functions to obtain the elastic displacement fields [Landau and Lifshitz (1986)]. Any unphysical divergences that are encountered in computing the elastic fields are avoided by using a cut-off length of 0.1 nm. The minimization is carried out using the a sequential quadratic programming method [Schittkowski (1986)].

The results for the optimized shapes obtained from two sets of parameters (β_0, β_1) = (15.5,1.6) and (14.65,4.13) meV/nm are given in Fig. 2.4. Thayer et al. [Thayer *et al.* (2004)] found that the measured bends approximately fit the former set of

parameters with smaller anisotropy in the boundary energy. However, we find that both sets of parameters provide reasonable fits to the experimental data, although the set with larger anisotropy is seen to be in better overall agreement with the measurements. In the range of sizes from 0.4 to 0.7 μm^2, where the error bars on the measurements are small, the shapes obtained for both cases are virtually indistinguishable. We have found that the measured data can also be fit with other pairs of parameters (β_0, β_1), but since the measured bends in the equilibrium shapes are small (few %), such a fit cannot unequivocally be used to determine the orientation dependence of the boundary energy. Note, however, that for large domain size (e.g. $A > 1$ μm^2), the equilibrium shapes are very different for the two sets of parameters [refer to Fig. 2.4(b) and 2.4(c)]. In principle, a measurement of the equilibrium shape at large size would greatly constrain the model parameters; however, a comparison between measured and calculated equilibrium shapes at large size is meaningless because *these equilibrium shapes are never observed in experiments.*

However, in what follows, we show that by analyzing the evolution of large domains far from equilibrium, we can more accurately determine the parameters (β_0, β_1). As we discuss next, we have implemented a dynamic model that allows us to predict how domains evolve with time for a given set of thermodynamic and kinetic parameters.

2.5 Phase field model for the shape evolution of surface domains on Si(111) surface

2.5.1 Formulation of the model

Consider a strained (7×7) reconstructed surface stress domain on a (1×1) reconstructed Si(111) surface as shown in Fig. 2.5. We model the dynamics of the shape evolution of the domain using Cahn-Hilliard phase-field equations [Eggleston *et al.*

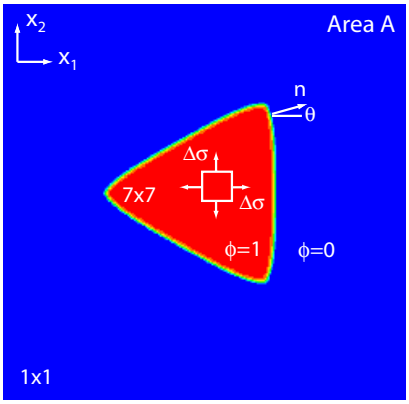

Figure 2.5: Schematic of the phase-field model for the growth of a strained (7×7) reconstructed surface domain on (1×1) reconstructed Si(111) surface. The phase-field order parameter ϕ takes the values $\phi = 0$ and $\phi = 1$ in the (1×1) and (7×7) phases, respectively, while varying smoothly from 0 to 1 in the narrow boundary region. $\Delta\sigma$ is the difference between the surface stresses of the (7×7) and the (1×1) phases. A, the combined area of the terrace and the domain is taken to be 92.16 μm^2 in the simulations.

(2001), Lu and Suo (2001)]. A conserved phase-field parameter $\phi(\mathbf{x}, t)$ is used to define the different surface 'phases' : $\phi = 0$ corresponds to the (1×1) phase and $\phi = 1$ for the (7×7) phase, while varying smoothly from 0 to 1 in the narrow boundary region. The difference in surface stress between the two phases, $\Delta\sigma$, results in force monopoles at the domain boundaries, which give rise to the elastic deformation field $\mathbf{u}(\mathbf{x}, t)$ on the surface and in the bulk substrate. The total free energy of the system of in Fig. 2.5 can be written as

$$E = \int_A \left(g(\phi) + \epsilon(\theta)^2 |\nabla\phi|^2 \right) dA - \frac{\Delta\sigma}{2} \int_A \mathbf{u} \cdot \nabla\phi \, dA \,. \tag{2.2}$$

The first term is the energy density of the domain and the terrace given by a double-well potential $g(\phi)$ (determined by the parameter K) with minima at $\phi \approx 0$ and $\phi \approx 1$ as,

$$g(\phi) = K\phi^2(1-\phi)^2 - \Delta\gamma(1-\phi)^2 \tag{2.3}$$

where $\Delta\gamma$ denotes the difference in surface energy between the (7×7) phase and the (1×1) phase. The second term in Eq. 2.2 involving the surface gradients of phase-field parameter ϕ denotes the energy of the domain boundary, where ϵ is the function of $\theta = \tan^{-1}(\phi_{x2}/\phi_{x1})$, the angle made by the outward normal to the domain boundary with x_1 direction as shown in Fig. 2.5. The connection between $\epsilon(\theta)$ and the boundary energy $\beta(\theta)$ can be obtained by demanding that the first two terms in Eq. 2.2 should reduce to the first term in Eq. 2.1 in the limit of a sharp-interface when $\Delta\gamma = 0$. This yields the relation [Eggleston *et al.* (2001)]

$$\epsilon(\theta) = \frac{3}{\sqrt{K}}\beta(\theta)\,. \tag{2.4}$$

The third term in Eq. 2.2, which denotes the elastic energy of the system, reduces to the second term in Eq. 2.1 when the interface is sharp. It was shown that the evolution of domain shape during growth is diffusion-limited – material transport via the diffusion of adatoms created on the surface by thermal generation is required for the movement of the domain boundaries [Hannon *et al.* (2000)]. Using M to denote the mobility for surface diffusion of adatoms, the equation governing the evolution of the phase-field order parameter (and hence the domain shape) can be written as

$$\frac{\partial\phi}{\partial t} = M\nabla^2\mu + f \tag{2.5}$$

where $\mu = \delta E/\delta\phi$ is the local chemical potential on the surface and f is the rate of creation of vacancy/adatom pairs (in ML/sec). Here we have assumed that the adatom concentration at the domain boundary is in local thermodynamic equilibrium, so that kinetics of motion of the domain boundary is essentially limited by the surface diffusion of the adatoms. An explicit expression for the chemical potential μ can be

written using linear elastic Green's functions [Landau and Lifshitz (1986)] as

$$\mu = \frac{\partial g}{\partial \phi} + \frac{\delta}{\delta \phi}(\epsilon^2(\theta)|\nabla\phi|^2) - F_0 \int_A \frac{(\mathbf{x}-\mathbf{x}')\cdot\nabla'\phi}{|\mathbf{x}-\mathbf{x}'|^3}\, d\mathbf{x}' \,, \tag{2.6}$$

where $F_0 = (1-\nu^2)\Delta\sigma^2/(\pi Y)$, ν and Y being the Poissons ratio and Youngs modulus, respectively.

As noted above, all the parameters in the phase-field model can be related to their sharp-interface counterparts [Eggleston *et al.* (2001)]. Numerical evolution of the phase-field equation (Eq. 2.5), however, is carried out much more efficiently than the time evolution of the corresponding sharp interface equation, particularly for the highly-branched shapes shown in Fig. 2.2. We have solved the governing phase-field equation using a semi-implicit Fourier spectral method in a periodic domain [Zhu *et al.* (1999)]. We now turn to a discussion of the numerical parameters chosen to model the dynamics of strained (7×7) domains.

2.5.2 *Numerical parameters in the phase-field model*

The key numerical parameters in the phase field formulation, K, M and $\epsilon(0)$, provide definitions for the following length and time scales:

$$l^* = \epsilon(0)/\sqrt{K} \quad \textit{and} \quad t^* = {l^*}^2/(KM)\,. \tag{2.7}$$

The relation of the length scale l^* to the elastic cut-off δ in the sharp-interface can be obtained by comparing the ratio of the elastic energy to the boundary energy of a strained domain of a simple shape. When the boundary energy is isotropic with value β, this ratio in the sharp interface model for a circular domain of radius R can

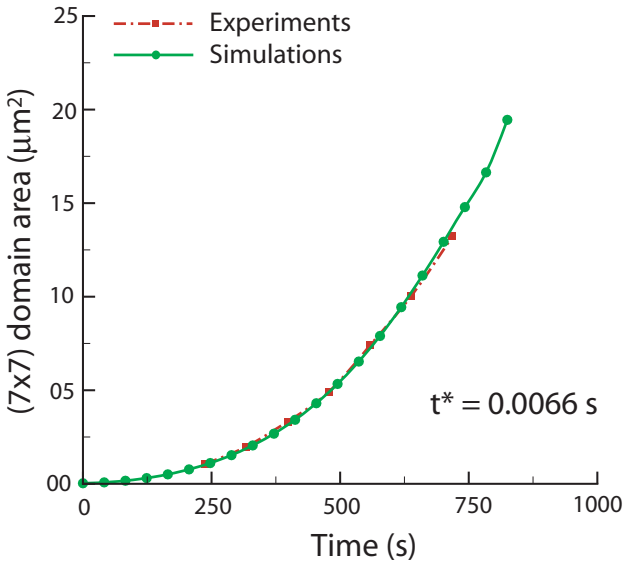

Figure 2.6: Area vs. time for the growth of (7×7) domains: experiments (red) and simulations (green). With time scale $t^* = 0.0066$ s, the rate of growth in simulations is in excellent agreement with the experiments.

be written in closed form as

$$r = -\frac{F_0}{\beta} \log[(8R/\delta) - 2] \,. \tag{2.8}$$

By computing the ratio r for circular domains of different radii using phase-field calculations, we obtain the relation $\delta = 0.01067 l^*$. For $\delta = 0.1$ nm, we have $l^* = 9.375$ nm. For estimating the time scale t^*, we compare the area of a growing (7×7) domain from phase-field simulations with the area observed in experiments [Fig. 2.2(a)] as a function of time [refer to Fig. 2.6]. We find that excellent agreement between experiments and simulations is obtained when $t^* = 0.0066$ secs. Once the estimates for the length and time scale are obtained, other parameters in the simulation can be readily evaluated. The rate of adatom-vacancy pair creation $f = 0.2 \times 10^{-5}$ ML/time (in t^* units) used in the simulations corresponds to 3×10^{-4} ML/s, which is close to 2×10^{-4} ML/s as reported in [Hannon *et al.* (2000)]. The parameter K, which

characterizes the energy densities of (7×7) and (1×1) phases can be obtained using Eq. 2.4 and Eq. 2.7 as $K = 3\beta(0)/l^*$. For $\beta(0) = 14.65$ nm, $K = 4.7$ meV/nm^2. The difference between the free energy density of (7×7) phase and (1×1) phase is $\Delta\gamma = (\gamma_{7\times7} - \gamma_{1\times1}) = \Delta S(T - T_C)$ with $\Delta S = 0.01\ k_B$ per (1×1) cell [Hannon *et al.* (2002)] and using $\Delta\sigma = 30$ meV/A^2 [Twesten and Gibson (1994)], the parameter F_0 in Eq. 2.6 is found to be 4.9 meV/nm. Finally, an estimate of the mobility for surface diffusion of adatoms can be obtained as $M = l^{*2}/(Kt^*) = 2.83 \times 10^3$ nm^4/meV/s.

2.6 Morphological evolution of stress domains on Si(111)

2.6.1 Comparison of simulations and experiments during growth

The shape evolution of domains with large and small anisotropies in $\beta(\theta)$ considered in the analysis of equilibrium shapes (Sec. 2.4), computed with the dynamic phase-field model for identical growth conditions, is shown in Fig. 2.7(b) and Fig. 2.7(c) and in movies S4 and S5,[2] respectively. For small size, the shapes of the domains are similar for both sets of parameters; however, when the domains are large, the shapes are remarkably different. If the anisotropy in $\beta(\theta)$ is large, the domain develops notches, leading to a serrated boundary [refer to Fig. 2.7(b)]. When $\beta(\theta)$ is more isotropic, the domain adopts a highly-curved triangular shape with three narrow arms [refer to Fig. 2.7(c)]. Clearly, the anisotropy in the boundary energy plays a crucial role in how the domain shape develops: when the anisotropy is small, the domains remain compact for larger sizes, whereas when the anisotropy is large, the

[2]Movies showing simulations of morphological evolution during growth can be down-loaded from http://nikhil.medhekar.googlepages.com/movies

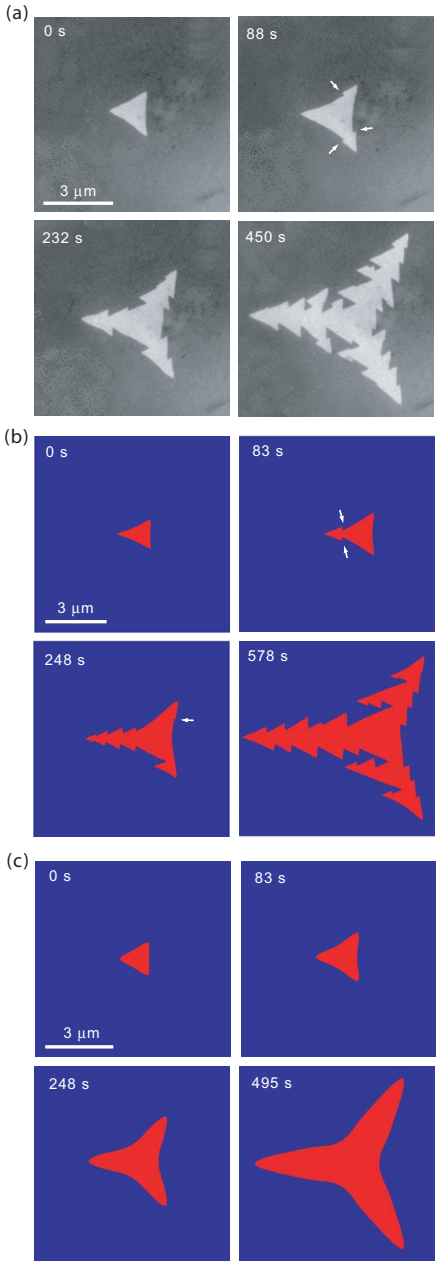

Figure 2.7: Growth of stress domains on Si(111): Comparison of experiments and phase-field simulations. (a) Sequence of 10 eV bright-field LEEM images. (b-c) Growth shapes of strained domains calculated using the dynamic growth model with large [given in (b)] and small [given in (c)] anisotropy in the boundary energy, $\beta(\theta)$. Note that the domain with larger anisotropy in boundary energy [given in (b)] develops serrations similar to the ones seen in experiments. Also, the side-branches in (a) and (b) first originate at the points of inflection, located nearly midway between the corners and the center of a side (marked by arrows).

domains can change their shape by formation of many small notches. The simulations show that larger anisotropy gives a better description of the growth observed in experiments.

To understand the conditions under which serrated boundaries form, it is useful to study the stability of the domain boundaries against the formation of a notch. Of particular interest is the location of the points along the boundary where such perturbations can grow. In the absence of strain, growth of a small perturbation on the boundary is determined by the boundary stiffness, $\tilde{\beta}(\theta) = \beta(\theta) + \beta''(\theta)$; orientations for which $\tilde{\beta}(\theta) > 0$ are stable, whereas unstable growth of the notch is possible when $\tilde{\beta}(\theta) < 0$ [Wulff (1901)]. In the presence of strain, an appropriate stability condition can be obtained by considering the critical wavelength for the growth of small amplitude sinusoidal perturbations applied to the boundary. A straightforward generalization of the result for boundaries with isotropic boundary energy shows that in the anisotropic case, only those perturbations whose wavelength is larger than the critical value,

$$\lambda_c = \delta \exp(\tilde{\beta}(\theta)/F_0) \tag{2.9}$$

grow in amplitude, while others decay [Leonard and Tersoff (2003)]. In Eq. 2.9, δ is the elastic cut-off length and $F_0 = (1-\nu^2)\Delta\sigma^2/(\pi Y)$, where Y and ν are the Youngs modulus and Poissons ratio, respectively. This result shows that for the orientations for which $\tilde{\beta}(\theta) < 0$, the critical wavelength is of the order of, or smaller than the elastic-cutoff length, which in turn is comparable to an atomic spacing. Since this length scale represents a lower bound on the wavelengths of the perturbations accessible to the boundary, orientations for which $\tilde{\beta}(\theta) < 0$, are unstable to the growth of a small notch. In this regard, the instability criterion for strained domains is similar to the corresponding criterion for the unstrained case.

The key difference between the two forms of boundary energies considered in the

analysis of equilibrium shapes relates to the behavior of stiffness $\tilde{\beta}(\theta)$ – in the case of the boundary energy with smaller anisotropy, $\tilde{\beta}(\theta) > 0$ for all orientations, while for the case with larger anisotropy, $\tilde{\beta}(\theta) < 0$ for orientations in the range $41^\circ < |\theta| < 60^\circ$. Furthermore, in the latter case, orientations in the range $24^\circ < |\theta| < 60^\circ$ are absent from the classic Wulff shape which minimizes the boundary energy of the domain in the absence of strain [Wulff (1901)]. In a thermodynamic sense [Williams and Bartelt (1991)], the total free energy of the domain can then be lowered by eliminating these 'unstable' orientations in favor of stable orientations that fall outside this range. The presence of unstable orientations leads to very different growth shapes for the two parameter sets. For the low-anisotropy parameter set, the boundary stiffness is always positive, and the boundaries can acquire very large concave curvatures without encountering any unstable orientations. This is indeed what is seen in both the growth and equilibrium shapes in this case, where large domains develop highly curved and elongated arms [refer to Fig. 2.4(b) and Fig. 2.7(c)]. The elongated shape in Fig. 2.4(b) has been observed by Grutter and Durig [Grutter and Durig (1995)] for epitaxially strained monolayer Co islands grown on Pt(111).

In contrast to shape evolution in the case of the low-anisotropy parameter set, for domains with large anisotropy in $\beta(\theta)$, there is a limit to the strain-induced concave bending that can be accommodated without encountering unstable orientations. As the domains grow in size, these orientations are first expected to appear at the points of inflection. At these points, the boundary orientation, $\theta(s)$, attains a local maximum at these points since curvature $= d\theta/ds = 0$. For shapes with concave bends, these points are located nearly midway between the corners and the center of the sides of a domain (marked by arrows in Fig. 2.4 and Fig. 2.7). In our growth simulations, notches form when the domain area reaches 2.7 μm^2, which is close to the size 3.0 μm^2, where serrations first appear in experiments. The locations where the notches

appear in experiments also coincide with points of inflection [refer to Fig. 2.7(a)]. Thus the growth simulations show that shapes with smaller anisotropy can remain unserrated even when their sizes are very large, whereas notches appear in domains with larger anisotropy at a critical size. The parameter set with large anisotropy in $\beta(\theta)$ therefore provides an excellent description of both the equilibrium shapes at small sizes and the serrated shapes observed during growth.

The side-branches do not appear on all the edges at the same time due to small thermal fluctuations in experiments. A similar effect is observed in our simulations due to unavoidable noise associated with finite precision numerics. Faster growth leads to pine-tree like morphology with many side-branches [Fig. 2.7(a,b) and movie S1], whereas slower growth results in the formation of fewer side branches [Fig. 2.2(b) and movie S3]. We can understand this by noting that during surface diffusion mediated growth, regions with high convex curvatures grow at a faster rate due to larger adatom concentration gradients in their vicinity [Mullins and Sekerka (1963)]. In the present case, large growth rates lead to faster growth of the corners, particularly after the formation of the first side-branch. The rapid outward movement of the corners and simultaneous strain-induced bending of the boundaries results in the appearance of unstable orientations, which in turn give rise to formation of serrations in rapid succession as seen in experiment [Fig. 2.7(a)] and simulation [Fig. 2.7(b)]. Annealing of highly serrated pine-tree like shapes or very slow growth from compact shape, on the other hand, leads to the connected-triangle morphology, as we discuss next.

2.6.2 Comparison of simulations and experiments during annealing

In Fig. 2.8(a) (also refer to movie S2), we show the shape evolution of three domains that are equilibrated at nearly fixed temperature for 800 seconds. As the

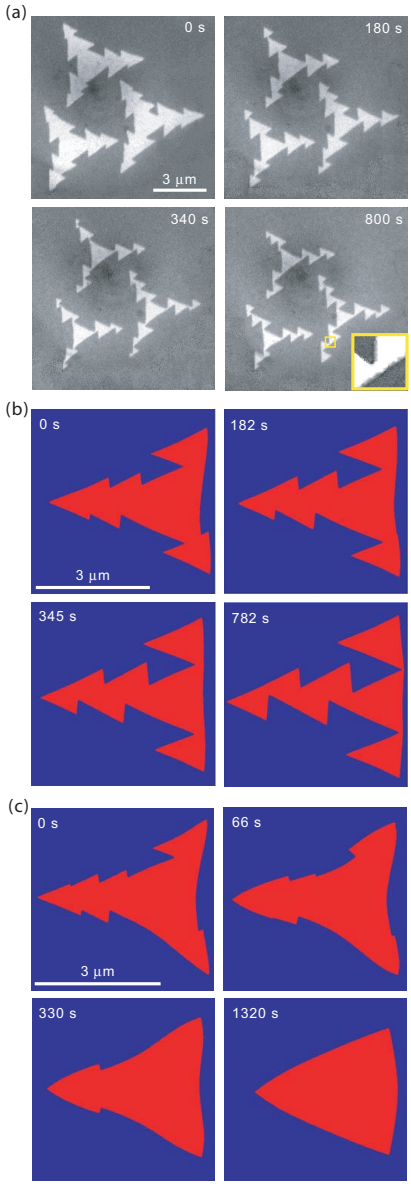

Figure 2.8: Annealing of stress domains on Si(111): Comparison of experiments with phase-field simulations. (a) Sequence of 10 eV bright-field LEEM images. The inset shows an enlarged view of a 0.5 μm $\times$ 0.5 μm area in the vicinity of the isthmus connecting two triangles. (b) The sequence of images from numerical simulations shows the equilibration of a branched shape with large anisotropy in $\beta(\theta)$. Note that the shape of the branched domain evolves to the assembly of connected triangles observed in experiment. (c) To contrast the shapes in (a) and (b) with the equilibrium shapes in an unstrained system, we have equilibrated the branched domain in (b) at constant area, by setting the surface stress difference, $\Delta\sigma = 0$. Unlike the shape evolution in (a) and (b), the concave corners move in an outward direction due to the Gibbs-Thomson effect, which eventually leads to the convex Wulff shape.

equilibration proceeds, the concave corners move inward towards the centers of the domains, so that the serrated shape is transformed into an assembly of connected triangles. Here, after a rapid shape transformation during a period of 100 sec, the equilibration is very slow with little change in area from 300 sec and 800 sec. Our simulations [Fig. 2.8(b)] also predict similar shape transformations during the equilibration of a large branched domain. As in the experiments, the inward movement of the corners can be attributed to strain – in the absence of strain, the Gibbs-Thomson effect would lead to an outward movement of these corners, which then results in a single compact island seen in Fig. 2.8(c).

A similar morphology of connected triangles is also obtained by very slow growth starting with a small, compact domain as shown in Fig. 2.2(b). This connected-triangle morphology cannot break-up into smaller domains because of the large energy barrier involved in pinching-off the isthmus [shown in the inset in Fig. 2.8(a-b)] that connect the nearly-triangular sub-domains at their vertices. The energy barrier arises from the large repulsive elastic interactions between the two sides of the isthmus, particularly at its neck. Typically, the distance between the tip of the V-groove and the straight edge in the inset in Fig. 2.8(a) is between 20 and 60 nm. Since the energy cost of reducing the width of the isthmus from 20 nm to 1 nm is 500 meV, thermal fluctuations of the boundaries (which are about 1-5 nm) cannot lead to the pinching of the isthmus. Since long-range interactions always hinder pinching, the observed behavior should be generic in the self-assembling systems where the thermal fluctuations of boundaries are small.

The key to understand why large domains eventually adopt the morphology of connected triangles with approximately equal area during slow growth [Fig. 2.2(b)] or annealing [Fig. 2.2(c)] is the notion of *metastability* in the domain shapes. In the next chapter (Chapter 3), we will discuss how an interplay between long-range elastic

interactions and crystalline anisotropy can give rise to a variety of long-lived and metastable domain shapes on cubic (111) surfaces.

2.7 Chapter summary

In summary, we have used real-time electron microscopy to image the growth of stress domains far from equilibrium. By comparing the observed domain shapes with a dynamic model, we have developed a quantitative understanding of the growth conditions that lead to notch formation. We have shown that although the formation of notches or serrations can lead to a lowering of elastic energy, this process is not 'universal', in the sense that it is observed only for a restricted class of boundary energies. When the anisotropy in the boundary energy is small, notches do not form since unstable boundary orientations are not encountered during growth. On the other hand, concave bending of domain boundaries can be considered to be universal as it is seen in strained domains with and without unstable orientations.

Furthermore, the arguments presented in this chapter show that conclusions solely drawn from the analysis of equilibrium shapes can be erroneous – consideration of growth shapes that show spontaneous formation of side-branches was essential to establish the presence of unstable boundary orientations. The features critical for these mechanisms, namely, anisotropy and long-range interactions (electrostatic, magnetic or elastic) are always present in any self-assembling system on crystal surfaces (for example, epitaxial nanowires, alloy films, strained quantum dots, ferromagnetic and ferroelectric memories/domains and stripe phases in superconductors). Our results should therefore be generic and find broad applicability in a variety of material systems.

Chapter 3

Metastability in 2D self-assembling systems

3.1 Introduction

The study of shapes of crystals has received considerable attention since the early work of Wulff [Wulff (1901)] as it provides quantitative information on the energetics and kinetics of surface processes. Shapes of crystalline nanostructures can also strongly influence their functional (e.g., electrical and optical) properties. According to the classic construction of Wulff [Wulff (1901)], the shapes of unstrained crystals in equilibrium are (1) independent of size, (2) always convex, and (3) unique, in the sense that for a given azimuthal dependence of the surface energy, there is a unique shape that minimizes the free energy of the crystal. More recent work has shown that long-range interactions due to elastic, electrostatic, or magnetic effects can complicate this simple picture. In particular, detailed studies of the shapes of 3D crystalline inclusions and quantum dots, 2D surface-stress domains and nanoislands, and epitaxial nanowires have clearly established the size dependence of equilibrium shapes

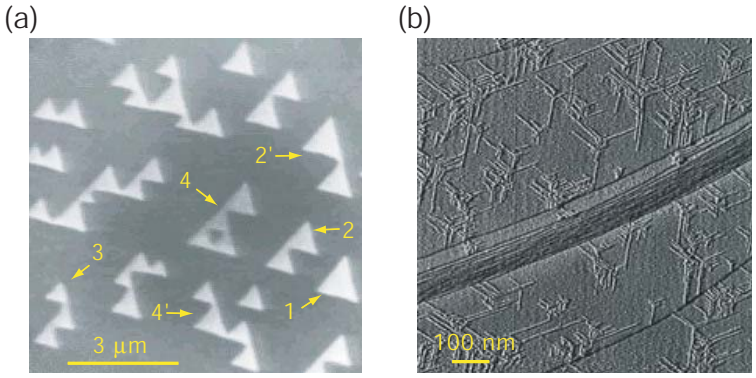

Figure 3.1: (a) LEEM images of (7×7) reconstructed domains on a (1×1) reconstructed Si(111) surface. The domain boundaries are oriented along ⟨110⟩. The areas of the domain marked 1, 2, 2', 3, 4, 4' are 0.76, 0.78, 1.33, 0.72, 1.31, and 1.32 μm^2, respectively. (b) STM image of Co islands on Pt(111), with epitaxial mismatch strain of 9 % [Grutter and Durig (1995)]. The three arms of Co islands are 3-5 nm wide and up to 250 nm long. They run *perpendicular* to the close-packed ⟨110⟩ orientations.

in strained systems.

In case of 2D self-assembling systems, two types of strain-induced shape transitions have been identified:

1. first-order transitions that involve elongation of initially symmetric shapes (squares or circles) along low-energy crystalline directions beyond a critical size [Tersoff and Tromp (1993), Brongersma *et al.* (1998), Li *et al.* (2000), van Gastel *et al.* (2006)] and

2. continuous evolution of stress domains from convex Wulff-like shapes at small sizes to shapes with concave boundaries at large sizes [Thayer *et al.* (2004)].

However, more intriguing shape transitions that do not fall under the two classes described above have also been reported on cubic (111) surfaces widely employed in epitaxial growth. Examples include the connected domain configuration of surface stress domains on Si(111) [Fig. 3.1(a)] and elongated shapes of Co islands on Pt(111)

with arms that run along high energy crystallographic orientations [Fig. 3.1(b)] [Grutter and Durig (1995)]. Furthermore, as seen in the previous chapter (Chapter 2), large annealed stress domains on Si(111) have always been found to adopt a peculiar morphology of connected triangles of approximately equal size (refer to Fig. 3.2).

Motivated by experimental observations of domain shapes on cubic (111) surfaces, we develop a unified description that elucidates and systematically classifies all the possible strain-stabilized shapes in this system. We find that the interplay between elastic relaxation and crystalline anisotropy on these material surfaces gives rise to a large variety of novel shapes not found on their (001) counterparts [Tersoff and Tromp (1993), Brongersma *et al.* (1998), Li *et al.* (2000)]. A key result of this work is the observation that almost all the shapes observed in experiments are not true equilibrium shapes, in the sense of being the *global* minimizers of the total energy, but are configurations trapped in shallow *metastable* minima. Subsequently, for a given size, a unique equilibrium shape will not always be obtained in the presence of strain.

The organization of the rest of the chapter is as follows. Sec. 3.2 briefly describes the wide variety of shapes that are observed in experiments on (111) surfaces. In Sec. 3.3, we revisit the analysis of equilibrium shapes of compact domains with different degrees of anisotropy in the boundary energy. Sec. 3.4 introduces the notion of metastability of equilibrium shapes based on the energy per unit area of these shapes. In Sec. 3.5, we explicitly map out the energy landscape for strain-induced shapes and present a phase diagram that shows all the possible metastable configurations as a function of the size of the self-assembled domains. Finally, the conclusions drawn from our analysis are presented in Sec. 3.6.

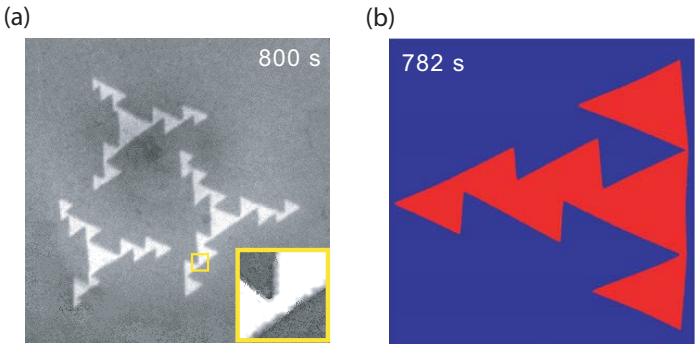

Figure 3.2: Connected-triangle morphology of annealed stress domains on Si(111). (a) 10 eV bright-field LEEM image and (b) Phase-field simulation. All connected triangles have approximately equal size.

3.2 What is an equilibrium shape?

Some of the intriguing shapes of strained domains and islands found on (111) surfaces are given in Fig. 3.1. Figure 3.1(a) is an image of an array of (7×7) reconstructed domains on a (1×1) reconstructed Si(111) held in equilibrium at 864 °C. As discussed in the previous chapter (Chapter 2), a difference in surface stress between the two reconstructions ($\Delta\sigma = \sigma_{7\times7} - \sigma_{1\times1}$) plays an important role in the formation and stability of the (7×7) domains [Hannon *et al.* (2002)]. While earlier studies [Thayer *et al.* (2004)] have considered the equilibrium shape of isolated compact domains [1 in Fig. 3.1(a)], other extended shapes with smaller triangular domains connected at their corners [refer to Fig. 3.1(a) and Fig. 3.2] can also be held without any noticeable change in shape for over 20 min. Furthermore, the sizes of many of these topologically distinct shapes with different numbers of connected triangles are nearly equal. This raises the question as to whether there is a unique 'equilibrium' shape for a given domain size.

Unlike the domains on Si(111) surfaces, strained Co islands on Pt(111) [Grutter and Durig (1995)] adopt an entirely different shape. While the domain boundaries in the former case are oriented along the close-packed ⟨110⟩ directions, highly elongated

arms of the Co islands run perpendicular to these low-energy orientations [refer to Fig. 3.1(b)]. How can we understand these distinct shapes within a unified framework? In what follows, we show that all these shapes are obtained from a simple functional form of the boundary energy as the degree of anisotropy in boundary energy is allowed to vary.

3.3 Analysis of equilibrium shapes of islands on (111) surfaces

First, we revisit the equilibrium shapes of compact domains on (111) surfaces with three-fold symmetric boundary energy of the form, $\beta(\theta) = \beta_0[1 + \alpha(1 - \cos(3\theta))]$, where θ denotes the angle made by the outward normal to the boundary with the horizontal axis and α is the parameter that determines the degree of anisotropy. The total energy of a strained domain can be written as

$$E(A) = \int_s \beta(\theta)\, ds - \frac{1}{2}\Delta\sigma \int_s \mathbf{n}(s) \cdot \mathbf{u}(s)\, ds \ , \tag{3.1}$$

where the integrals are taken over the perimeter of the domain, $\Delta\sigma$ is the difference in the surface stresses or the product of the mismatch stress and the height of the islands in the case of coexisting domains or strained monolayer islands, respectively, and $\mathbf{u}$ denotes the elastic displacement fields. Using typical values $\beta_0 = 15.48$ meV/nm, $F_0 = (1-\nu^2)\Delta\sigma^2/(\pi Y) = 2.853$ meV/nm (where ν is Poissons ratio and Y is Youngs modulus) and an elastic cutoff parameter $\delta = 0.1$ nm [Hannon *et al.* (2002)], we have obtained the equilibrium shapes by minimizing the total energy using a sequential quadratic programming method [Schittkowski (1986)]. The displacement fields $\mathbf{u}$ are computed using surface elastic Green's functions [Landau and Lifshitz (1986)]. The computed shapes for three different values of α are shown in Fig. 3.3.

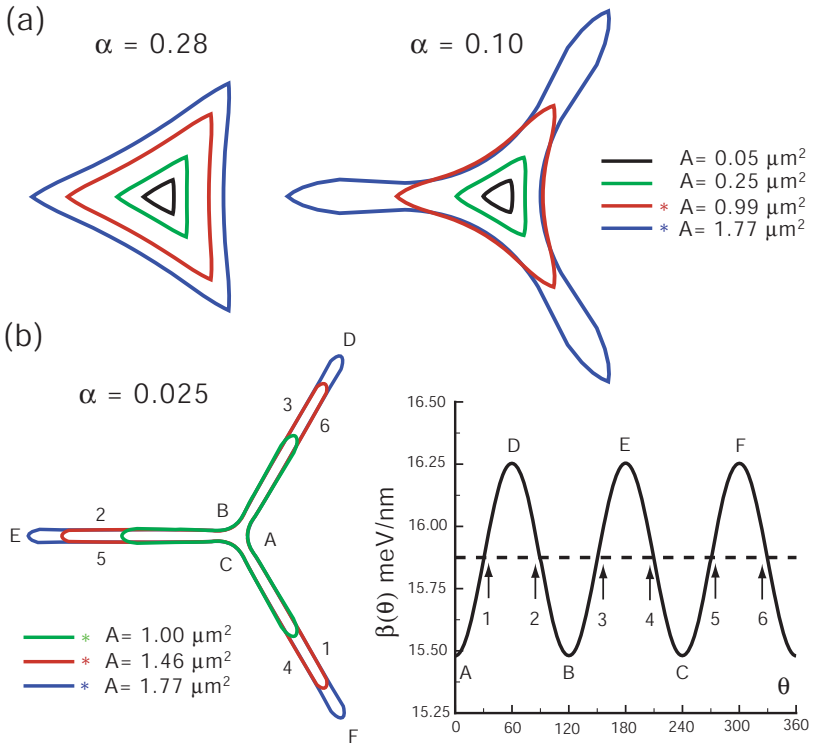

Figure 3.3: Equilibrium shapes of domains on (111) surfaces given for three different values of the anisotropy parameter, α. For large anisotropy in boundary energy, domain boundaries are nearly straight, while for smaller anisotropy, boundaries assume large concave curvatures. The domains marked with the asterisk(*) are in metastable equilibrium. The width of the side-arms is independent of domain size. The inset in (b) shows the plot of $\beta(\theta)$ with three minima and three maxima labeled A-C and D-F, respectively, and six intermediate orientations labeled 1-6. These orientations are also shown in the equilibrium shapes in (b).

With increasing domain size, the domain boundaries continuously bend towards the center, so that large domains acquire concave boundaries as reported in [Thayer *et al.* (2004)]. When the anisotropy becomes smaller, it becomes easier for the boundaries to bend as this leads to efficient relaxation of strain. For the case $\alpha = 0.025$, even at small sizes, the boundaries curve inward to the fullest possible extent until they acquire straight and narrow arms shown in Fig. 3.3(b). Unlike the shapes for large anisotropy in Fig. 3.3(a), with increasing size, domains in this case show shape

invariant growth with constant widths of the side arms. By analytical minimization of the total energy, the width w can be written in a closed form as

$$w = 2a \exp\left(\frac{\alpha\beta_0}{F_0} + \frac{1}{1-\nu}\right), \tag{3.2}$$

where $a = \delta \exp(\beta_0/F_0)$. The widths of the numerically computed shapes in Fig. 3.3(b) closely agree with this expression.

On a (111) surface the orientations of the six sides of the long arms in Fig. 3.3(b) correspond to $\langle 112 \rangle$ directions – the boundary energy of these orientations is intermediate between the three low-energy $\langle 110 \rangle$ orientations (A-C) and the other $\langle 110 \rangle$ orientations (D-F) which have the largest boundary energy. The elongated shape therefore involves a significant compromise between the boundary energy (which increases by over 200% relative to the classic Wulff shape) and the relaxation of the elastic energy. This shape predicted by our analysis agrees well with the observed elongation of the arms (that run along $\langle 112 \rangle$) for strained monolayer Co islands on Pt(111) in Fig. 3.1(b). Since the mismatch strain in this material system is large (9.7%), other strain relaxation mechanisms such as defect or dislocation formation have also been observed at very large domain sizes [Grutter and Durig (1995)]; further quantitative work is needed to obtain the relative importance of the different relaxation mechanisms.

3.4 Metastability – energy per unit area of domains

It is evident from Fig. 3.3 that a wider range of shapes are obtained on (111) surfaces compared to (001) surfaces [Tersoff and Tromp (1993), Brongersma *et al.* (1998), Li *et al.* (2000)]. However, the most significant difference between the two

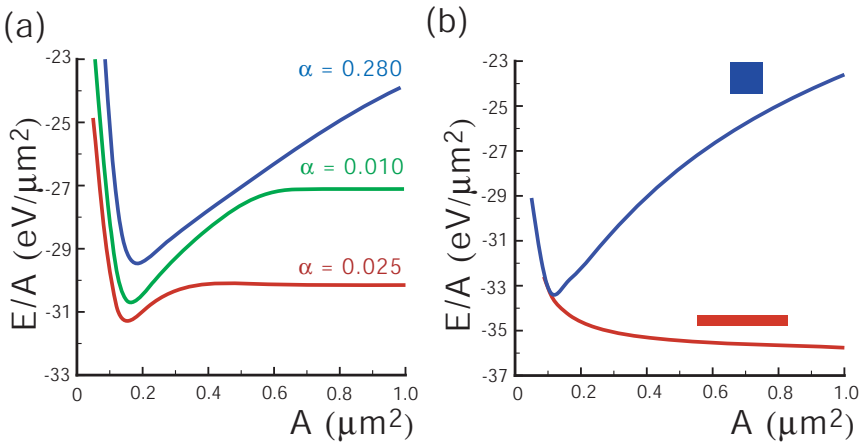

Figure 3.4: Energy per unit area for: (a) domain shapes on a cubic (111) surface given in Fig. 3.3, and (b) square and rectangular domains on a (001) surface [Li *et al.* (2000)]. This quantity attains minimum for the compact domain of size 0.2 μm^2 on the (111) surfaces, while the elongated nanowire shape has *smaller* minimum energy per unit area on the (001) surface. Material parameters used in this calculation are $\beta_0 = 15.48$ meV/nm and $F_0 = 2.853$ meV/nm.

cases relates to the behavior of energy per unit area of the strain-stabilized shapes as plotted in Fig. 3.4. This quantity is minimum for the infinitely long nanowire shape for (001) surfaces but the minimum is located at a finite size ≈ 0.2 μm^2 for domains on (111) surfaces. Since the optimum size is nearly independent of anisotropy in $\beta(\theta)$, it can be estimated using the closed form expression for the total energy of a triangle as

$$A_0 = a^2\mu^2 \exp(2)\,, \tag{3.3}$$

where $\mu = 1.97\exp[1/(1-\nu)]$. For the parameters used in our analysis $A_0 = 0.18$ μm^2, which is close to the values obtained for all the three cases plotted in Fig. 3.4. This analysis shows that on (111) surfaces, any domain larger than the optimum size A_0 is metastable – the total energy of this domain can be lowered by breaking it up into $N \approx A/A_0$ smaller domains. As we show below, this process, however, involves a large energy barrier and therefore the shapes marked by the * in Fig. 3.3 remain

trapped in metastable wells. In distinct contrast, the elongated nanowire shape on (001) surfaces corresponds to the global minimum of the total energy.

3.5 Energy barriers and morphological phase diagrams

If an isolated domain has to break up into smaller domains, notches on the boundary have to first nucleate and grow. Here we focus attention on the energy landscapes (Fig. 3.5) for the growth of notches on straight triangles since the key features apply equally well to domains with curved boundaries. For small domains ($A < 2A_0$), notches never grow as this always leads to an increase in the total energy of the domain. However, for larger domains, it becomes favorable for a notch to grow [Fig. 3.5(a)], but only after the notch has reached a critical size. In other words, the notch has to overcome a barrier before it can access a new minimum with two connected triangles. The evolution of the domain shapes along the 'saddle path' for this case is shown in Fig. 3.5(a). When the domains become even larger, two notches can grow and lead to a new minimum consisting of three connected triangles as shown in Fig. 3.5(b). However, the domain in this case can also adopt a metastable configuration with two connected triangles. The saddle paths for moving between the different wells in the energy landscape are given in the inset in Fig. 3.5(b).

Although the total free energy of the connected domains can be further lowered by breaking them into a number of widely separated domains of area A_0, the domains in experiments [Fig. 3.1(a) and Fig. 3.2] as well as in our calculations (Fig. 3.5) always stay connected at the corners. The strong repulsive elastic interactions between the approaching groove and the straight edge prevents the individual domains from pinching off from the larger connected structure. The equilibrium distance between

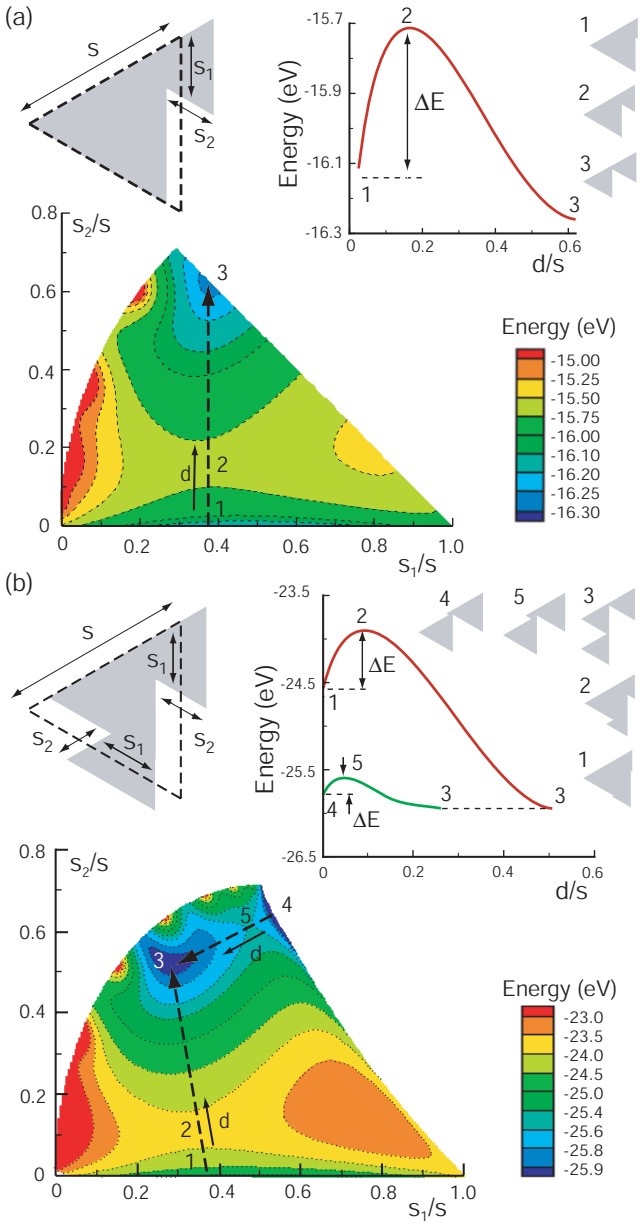

Figure 3.5: Energy landscapes for the growth of notches plotted as a function of their location (s_1) and lengths (s_2): (a) One notch on a domain with area 0.6 μm^2, and (b) Two notches on a domain with area 1.0 μm^2. Insets show the evolution of domain shapes and the corresponding energies along saddle paths. Material parameters used in the calculations, $\beta_0 = 15.48$ meV/nm, $C_0 = 2.853$ meV/nm correspond to the (7×7) domains on Si(111).

the V groove and the straight edges obtained from our calculations (50 nm) compares favorably with distances ($\sim$ 20-60 nm) found in experiments. Since repulsive long-range interactions between the approaching boundaries will always prevent pinching, the observed behavior should be generic [for example, see Plass *et al.* (2002)], but is particularly exaggerated in our experiments because of the small thermal fluctuation amplitudes.

A phase diagram that enumerates the most favorable shapes as a function of the normalized domain size and anisotropy is given in Fig. 3.6(a). We have obtained this phase diagram by comparing the total energy of shapes with different numbers of notches. This diagram, therefore, is a generalization of the landscapes in Fig. 3.5 for shapes with finite anisotropy in $\beta(\theta)$. Also, as in Fig. 3.5, while the shapes with $N \approx A/A_0$ connected domains is most favorable for a given area, A, other shapes with fewer connected-domains also remain metastable at all sizes. Transitions between the optimal shapes and the metastable shapes involves energy barriers, which are of the order of 0.3-0.7 eV for typical parameters used in our calculations. Clearly, these barriers can never be overcome by thermal fluctuations ($<$ 0.12 eV in most experiments). Thus, the final shape adopted by a domain will depend on the number of notches it possessed prior to equilibration. In particular, if there are no notches in the shape, very large isolated domains can remain trapped in metastable shapes given in the phase diagram in Fig. 3.6(b). Next, we show that these predictions are in agreement with experimental observations on Si(111).

In the case of in Fig. 3.1(a), the domains were first grown under non-equilibrium conditions that lead to the formation of different number of notches on each domain [Medhekar *et al.* (2007*a*)]. The final shapes in Fig. 3.1(a) were obtained by annealing the non-equilibrium shapes at 864 °C. According to our analysis, during annealing, depending on the number of notches in the initial shape, the domain should evolve

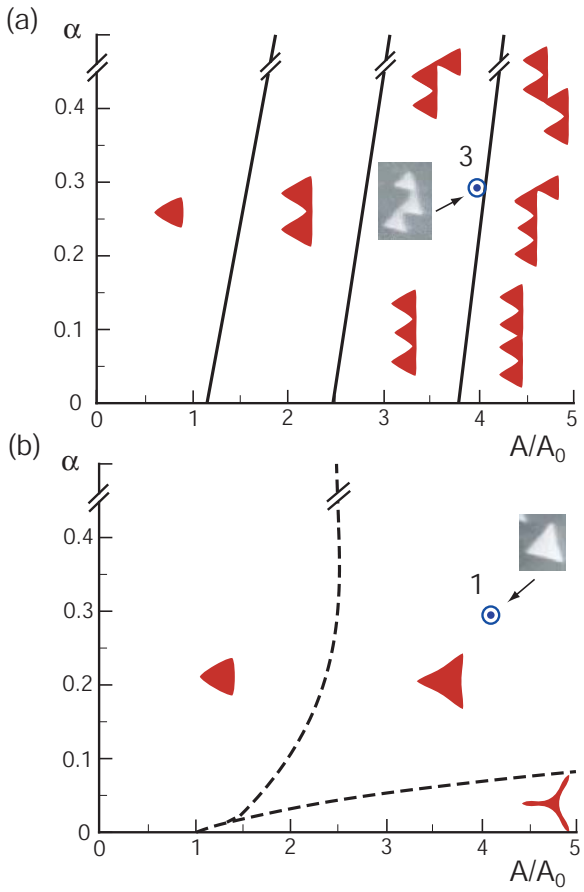

Figure 3.6: Morphological phase diagrams for strained domains on (111) surface as a function of normalized area A/A_o and anisotropy factor α. Part (a) shows optimum connected-domain shapes while part (b) shows the optimum shapes of an isolated compact domain. While energy barriers are encountered in crossing the phase boundaries in (a), the phase boundaries in (b) involve continuous transitions without any barriers. The energy difference between the different shapes with 3 and 4 connected domains is very small ($< 5\%$). Points marked 1 and 3 correspond to the Si (7×7) domains of nearly identical size in Fig. 1(a). Note that although the total energy of domain 3 is lower, the domain 1 is trapped in a metastable state. The anisotropy parameter for this material system is $\alpha = 0.28$ [Medhekar *et al.* (2007*b*)].

to the closest well in the energy landscape and remain trapped there irrespective of its size. This is indeed what is seen in experiment: while the domains marked 1, 2, and 3 in Fig. 3.1(a) are all of the same size, $A \approx 0.75\ \mu\text{m}^2$, they correspond to a compact, two-connected and three-connected shapes, respectively. Similarly for $A \approx 1.3\ \mu\text{m}^2$, we find a shape with two connected domains (2') as well as two shapes with four-connected domains (4 and 4'). These observations are therefore in complete agreement with the energy landscapes and phase diagrams shown in Figs. 3.5 and 3.6, respectively.

3.6 Chapter summary

In summary, we have shown that crystal symmetry plays a very important role in determining the energy landscapes for strained domains. We find significant qualitative differences in the equilibrium shapes on commonly used cubic (001) and (111) surfaces. While the global minimizer in the former case for a given area is a nanowire, in the latter case, it is an array of isolated domains of an optimum size that are widely separated from each other. We have shown here that this configuration is never achieved due to metastability induced by strain. We have presented morphological phase diagrams that predict the size dependence of various metastable shapes that have been observed in experiments. More insights into the interplay between strain and crystalline anisotropy can be gained by extending our analysis to equilibrium shapes on low-symmetry, high-index crystal surfaces.

Chapter 4

Shape dynamics in anisotropically strained 2D self-assembling systems

4.1 Introduction

Atomic and molecular self-assembly has attracted significant attention due to potential applications in non-lithographic fabrication [Whitesides and Grzybowski (2002)]. Of particular interest is the role of long-range elastic interactions which can induce spontaneous formation of structures like quantum dots [Ross *et al.* (1999), Drucker (2002)], two-dimensional (2D) periodic patterns and surface domains [Seul and Andelman (1995), Plass *et al.* (2001), Hannon *et al.* (2002)] and epitaxial nanowires [Sunamura *et al.* (1996), Evans and Nogami (1999), Chen *et al.* (2002), You *et al.* (2006), Owen *et al.* (2006), Sone *et al.* (2007), Lim *et al.* (2007), Li *et al.* (2007)]. Many such structures and patterns have nanoscale dimensions, making them suitable for application in photonic and memory devices and as nanoscale surface templates.

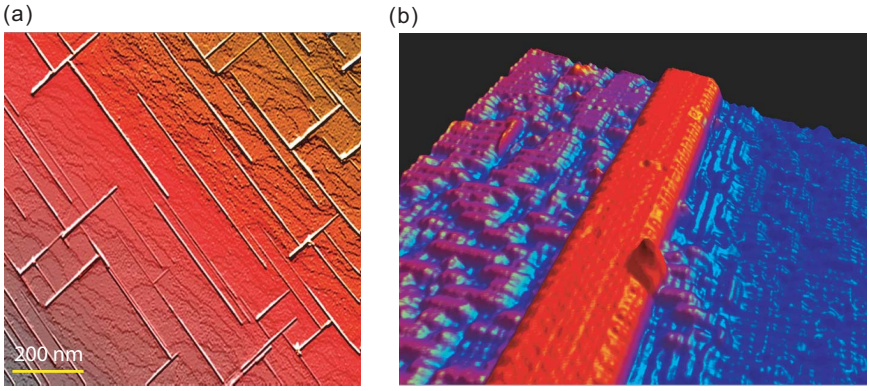

Figure 4.1: STM topographs of $ErSi_2$ nanowires grown on Si(001) Chen *et al.* (2002). A typical $ErSi_2$ nanowire is 9 atoms wide and 250 nm long. $ErSi_2$ has lattice mismatch of 6% and 1.5% along the two perpendicular $\langle 110 \rangle$ directions on Si(001) surface.

Further, as discussed in previous chapters (Chapters 2-3), elastic interactions control not only the long-range spatial arrangement, but also the shape of individual structures, which influences their functional (for example, electrical and optical) properties [Gangopadhyay and Nag (1997)]. For better control over the morphology and spatial patterning during processing and fabrication, it is therefore vital to understand key thermodynamic and kinetic mechanisms that govern strain-induced self-assembly in these systems.

The objective of this study is to analyze the shape evolution of strained 2D self-assembled nanostructures. In particular, we consider systems where the *anisotropy* in basic thermodynamic quantities like boundary free energy or mismatch strain results in intriguing shapes. Excellent examples of material systems where the mismatch strain is anisotropic are rare earth silicides ($ScSi_2$, $ErSi_2$, $DySi_2$ and $GdSi_2$) deposited on Si(001), where the magnitude of the lattice mismatch between epitaxial layer and substrate is large (6%-8%) along one of the crystallographic axes and small along the perpendicular direction (1%-2%) [Chen *et al.* (2002), You *et al.* (2006), Sone *et al.* (2007), Lim *et al.* (2007)]. The relaxation of mismatch strain leads to formation of

nanowires that have widths and lengths in the range of 5-15 nm and 250-400 nm, respectively. An example of such elongated nanowires is given in Fig. 4.1.

While most studies to date have focused on obtaining equilibrium shapes of strained structures [Tersoff and Tromp (1993), Li *et al.* (2000), Pradhan *et al.* (2004)], experiments have shown that kinetics plays an important role in shape evolution during growth [Li *et al.* (2007), Medhekar *et al.* (2007*b*)]. The primary mechanism for growth of these nanostructures is the surface transport of adsorbed or deposited species by thermally activated diffusion. If f and D denote the rate of deposition and surface diffusivity, respectively, then the ratio f/D characterizes a competition between the thermodynamics and kinetics of growth processes in a qualitative sense. When the deposition is slow compared to diffusion (small values of f/D), the evolution of the shapes is completely determined by the thermodynamics of the strained system. However, the shapes of the strained structures are increasingly controlled by kinetics as they are grown faster at low temperatures (large values of f/D).

In this chapter, based on a kinetic growth model, we study the shape dynamics of anisotropically strained 2D self-assembled structures. Our key results can be summarized as follows:

1. The aspect ratios of the shapes (defined as the ratio of length to width of the shape) depend strongly on the anisotropies in boundary energy and strain as anticipated from thermodynamics, but more importantly, we find that they depend also very strongly on the rate of growth. When anisotropy in mismatch strain is large, the aspect ratios of the shapes during growth are considerably *smaller* than the predictions of the equilibrium theory.

2. We find that the shapes obtained for the case where the principal components of the mismatch strain are equal in magnitude but opposite in sign (for example, monolayer islands on Si(001) [Zielasek *et al.* (2001)]) are characteristically

different from all other cases. In particular, the aspect ratios observed during growth are found to be *larger* than the corresponding equilibrium values. We show that this distinct behavior can be explained by a novel 4-fold symmetry in the shapes introduced by the relaxation of the anisotropic mismatch strain.

The rest of the chapter is organized as follows. In Sec. 4.2, we present the formulation of a dynamic growth model which accounts for the thermodynamics as well as kinetics of growth. In Sec. 4.3 and Sec. 4.4, we describe the shape evolution of epitaxial nanowires and stress domains on Si(001), respectively, grown under conditions that are close to and far from equilibrium. Finally, the conclusions drawn from our simulations are summarized in Sec. 4.5.

4.2 Dynamic Growth Model

4.2.1 Formulation of the model

Consider a planar, epitaxially strained island shown in Fig. 4.2. The equilibrium shape of this island can be obtained by minimizing its total free energy, $E = E_b + E_e$, where E_b is the energy cost of creating the island boundary given by

$$E_b = \int_s \beta(\theta)\, ds\,, \tag{4.1}$$

$\beta(\theta)$ being the orientation-dependent boundary free energy and E_e is the contribution of elastic energy to the total free energy, which can be written as

$$E_e = \int_{A_i} W^m\, dA - \frac{1}{2} h \int_s \sigma^m_{ij} n_j(s) u_i(s)\, ds\,. \tag{4.2}$$

The first term in Eq. 4.2 represents the strain energy in the island due to epitaxial mismatch, where $W^m = \frac{1}{2} h \sigma^m_{ij} \epsilon^m_{ij}$ is the uniform strain energy density, ϵ^m_{ij} and σ^m_{ij}

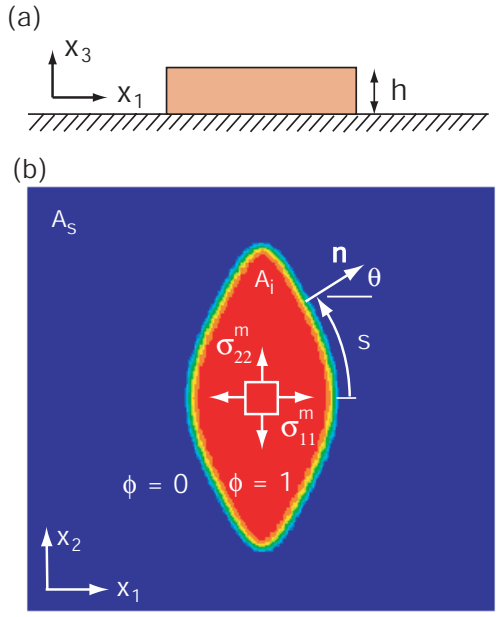

Figure 4.2: Schematic of a planar, epitaxially strained island. (a) Cross-sectional view in x_1-x_3 plane. h is the height of the planar island. (b) Phase-field model of the strained island. The order parameter ϕ takes values $\phi = 0$ and $\phi = 1$ on the terrace and in the island, respectively, while varying smoothly from 0 to 1 in the narrow boundary region. σ_{ij}^m is the in-plane stress due to elastic mismatch between the island and the substrate. A_i and A_s is the area of the island, and the terrace, respectively.

being the mismatch strain and the corresponding mismatch stress, respectively. The second term is the contribution due to the elastic relaxation at the island boundary, where u_i denotes the elastic displacement field.

In near-equilibrium growth conditions, the shapes are completely determined by thermodynamics (Eqs. 4.1-4.2). During kinetically limited growth, however, due to continuous incorporation of deposited adatoms that diffuse towards the island boundary, large islands have insufficient time to reach minimum-energy configurations, resulting in shapes that are out of equilibrium. To analyze the dynamics of shape evolution during growth, we have implemented a growth model based on phase-field equations that takes into account the kinetics of diffusion. As we discuss next,

this model accounts for the orientation dependence of the boundary energy and the anisotropy in strain.[1]

We model the dynamics of shape evolution of the strained island using Cahn-Hilliard phase-field equations [Cahn (1961), Eggleston *et al.* (2001), Lu and Suo (2001)]. A conserved order parameter $\phi(\mathbf{x}, t)$ is used to define the surface 'phases': $\phi = 0$ corresponds to the terrace phase and $\phi = 1$ to the island phase, while varying smoothly from 0 to 1 in the narrow boundary region. The expressions for the boundary energy and the elastic energy, which are equivalent to Eqs. 4.1-4.2 in the limit of a sharp interface, can be written as

$$E_b = \int_A \left(g(\phi) + \epsilon(\theta)^2 |\nabla \phi|^2 \right) dA \quad \text{and} \tag{4.3}$$

$$E_e = \int_A \left(W^m \phi + \frac{1}{2} \sigma_{ij}^m \phi_{,j} \, u_i \right) dA \,, \tag{4.4}$$

where $A = A_i + A_s$ is the combined area of the island and the terrace. The first term in Eq. 4.3 is the energy density given by a double well potential $g(\phi) = K\phi^2(1-\phi)^2$, with minima at $\phi = 0$ and $\phi = 1$. The second term in Eq. 4.3 involving surface gradients of the order parameter ϕ denotes the energy of the island boundary, where the coefficient ϵ is the function of $\theta = \tan^{-1}(\phi_{x_2}/\phi_{x_1})$, the angle made by the outward normal $\mathbf{n}$ to the boundary with x_1 direction. By demanding that expression for surface energy, Eq. 4.3, be equivalent to its sharp interface counterpart (Eq. 4.1), $\epsilon(\theta)$ can be related to the boundary free energy $\beta(\theta)$ as [Eggleston *et al.* (2001)],

$$\epsilon(\theta) = \frac{3}{\sqrt{K}} \beta(\theta) \,. \tag{4.5}$$

[1] The model developed here is similar to the model used to analyze far from equilibrium growth of stress domains on Si(111) (refer Chapter 2), except with an additional complexity arising due to the anisotropy in strain.

The first term in Eq. 4.4 corresponds to the uniform strain energy in the island, while the second term denotes the contribution due to the elastic relaxation at the island boundary.

As noted earlier, the shape of the island evolves due to diffusion of adatoms on the terrace and along the island boundary. The governing equation for the evolution of the order parameter (and hence the shape) can then be written as

$$\frac{\partial \phi}{\partial t} = \nabla \cdot (\mathbf{M} \nabla \mu) + f \,, \tag{4.6}$$

where $\mathbf{M}$ is the mobility, $\mu = \delta E / \delta \phi$ is the local chemical potential on the surface, and f is the rate of adatom deposition. Here we have assumed that the adatom concentration at the boundary is in local thermodynamic equilibrium, so that the kinetics of motion of island boundary is essentially limited by the surface diffusion of adatoms. The contribution to the chemical potential due to elastic relaxation can be computed using surface elastic Green's functions [Landau and Lifshitz (1986)]. In the case of equi-biaxial mismatch ($\sigma^m_{11} = \sigma^m_{22}$ and $\sigma^m_{12} = 0$), the chemical potential can be written in a relatively simple form as

$$\mu = W^m + \frac{\partial g}{\partial \phi} + \frac{\delta}{\delta \phi}(\epsilon^2(\theta)|\nabla \phi|^2) - F_0 \int_A \frac{(\mathbf{x} - \mathbf{x}') \cdot \nabla' \phi}{|\mathbf{x} - \mathbf{x}'|^3} \, d\mathbf{x}' \,, \tag{4.7}$$

where $F_0 = (1 - \nu^2) h^2 {\sigma^m_{11}}^2 / (\pi Y)$, ν and Y being the Poisson's ratio and elastic modulus, respectively. The mobility $\mathbf{M}$ in Eq. 4.6 assumes the value M_s for diffusion on surface and M_e diffusion along the island boundary. We solve the governing phase-field equation (Eq. 4.6) using a semi-implicit Fourier spectral method in a periodic domain [Zhu *et al.* (1999)].

4.2.2 Numerical parameters used in the model

The key numerical parameters in phase-field equations (Eqs. 4.3-4.7) provide the definitions of the length and time scales in the simulations: $l^* = 3\beta_0/K$, and $t^* = l^{*2}/D$, where $D = KM_S$ can be viewed as the surface diffusivity of adatoms. When the boundary of the island is treated as a sharp interface, the elastic fields become singular as one approaches the boundary. This singularity is usually regularized by using a cutoff length, which is typically of the order of 0.1-0.2 nm. By comparing the characteristic lengths to analytic expressions, a relationship between the length scale l^* and the elastic cutoff can be obtained. As discussed in detail later, the estimates for length and time scales will be obtained separately for nanowires and stress domains on Si(001).

Next we consider the shape evolution as a function of island size for both near-equilibrium and out-of equilibrium growth conditions. In particular, the limitations of slow kinetics are analyzed by varying rate of growth and the mobility for diffusion along the island boundary, M_e.

4.3 Nanowires on cubic (001) surfaces

We first consider the growth of epitaxial nanowires on (001) surfaces (such as rare-earth silicide nanowires on Si(001) [Chen *et al.* (2002), You *et al.* (2006), Sone *et al.* (2007), Lim *et al.* (2007)]) with two-fold symmetric shapes. The boundary energy $\beta(\theta)$ is modeled with a simple parametric form $\beta(\theta) = \beta_0(1 - \alpha\cos(2\theta)$, where α is the anisotropy factor. As noted earlier, the mismatch strain is anisotropic in these material systems. To analyze the influence of anisotropy in strain on island shapes, we consider two representative cases:

1. equi-biaxial elastic mismatch, $\sigma^m_{22}/\sigma^m_{11} = 1$ and $\sigma^m_{12} = 0$, and

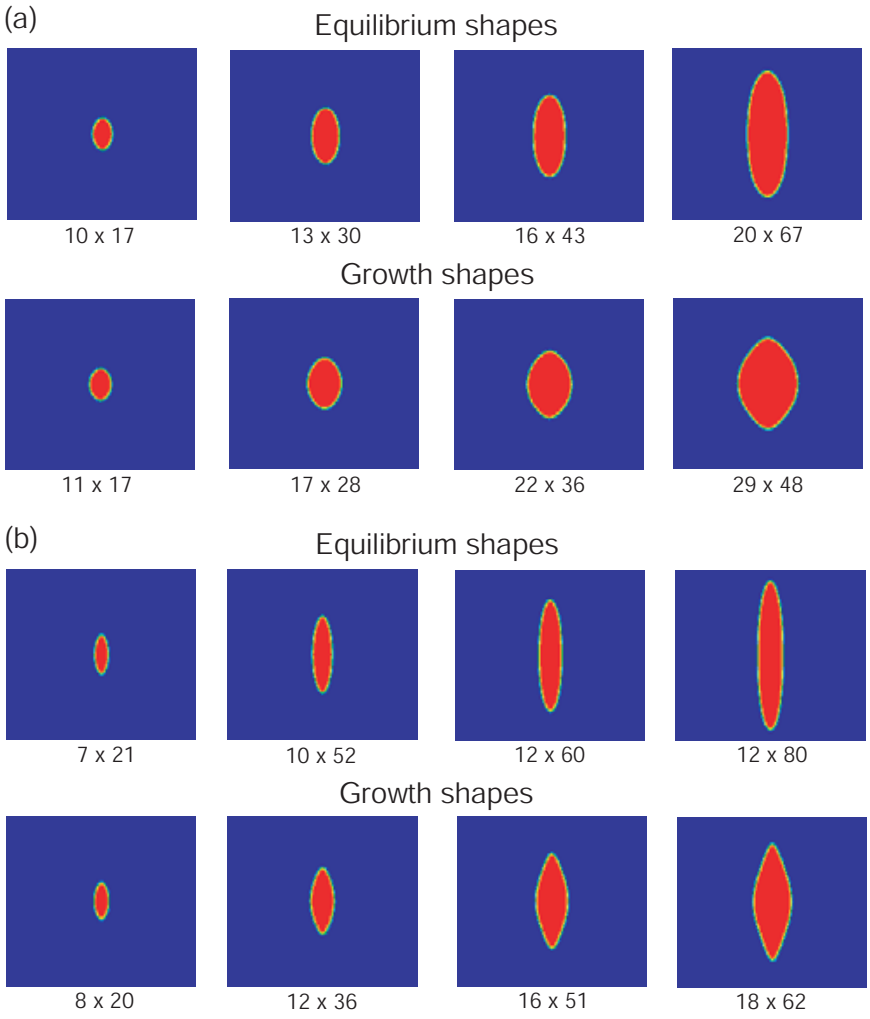

Figure 4.3: Equilibrium and growth shapes for (a) isotropic stress: $\sigma_{22}^m/\sigma_{11}^m = 1$ and (b) anisotropic stress: $\sigma_{22}^m/\sigma_{11}^m = 0.5$. Growth shapes are computed with $f = 0.25$ ML/s and $M_e/M_s = 0$. The dimensions marking each shape represent the lengths of minor and major axes in nm.

2. anisotropic elastic mismatch, $\sigma^m_{22}/\sigma^m_{11} = 0.5$ and $\sigma^m_{12} = 0$.

It is convenient to discuss the effect of strain on island shapes in terms of a dimensionless parameter F_0/β_0, where $F_0 = (1-\nu^2)h^2\sigma^2_{11}/(\pi\, Y)$, ν and Y being the Poisson's ratio and the elastic modulus, respectively. For $F_0/\beta_0 = 0.33$ and $\alpha = 0.1$, equilibrium and growth shapes for the two cases of elastic mismatch are given in Fig. 4.3, while Fig. 4.4 shows evolution of the aspect ratios. For a given island size, equilibrium shapes are computed by setting $f = 0$ in Eq. 4.6.

We find that with equi-biaxial as well as anisotropic mismatch strain, the islands grow in equilibrium primarily along their major axes while their widths quickly approach a constant level. Subsequently their aspect ratios increase as they grow in size. This behavior is consistent with theoretical predictions which show that a large strained island adopts an elongated wire-like shape which allows for efficient relaxation of strain [Tersoff and Tromp (1993), Li *et al.* (2000)]. For the case of equi-biaxial mismatch, an analytical expression for the width w of an infinitely long wire can be written as [Medhekar *et al.* (2007*a*)]

$$w = 2\,a\,\exp\left(\frac{1}{1-\nu}\right), \tag{4.8}$$

where $a = \delta\,\exp((1-\alpha)\beta_0/F_0)$. By comparing the width of wires shown in Fig. 4.3(a) with this expression, a relationship between the elastic cutoff length δ and the intrinsic length scale l^* in the phase-field simulations can be obtained as $l^* \approx 6.2\delta$.

The role of strain-driven elongation in nanowires is further evident when the strain is anisotropic. As seen in Fig. 4.3(b), the island in equilibrium grows preferentially in the less strained direction resulting in smaller width and larger equilibrium aspect ratios [Fig. 4.4(b)] compared to the case of equi-biaxial strain [Pradhan *et al.* (2004)]. The width of the nanowire computed with anisotropic epitaxial mismatch is comparable to the observed widths of silicide nanowires on Si(001). However, in

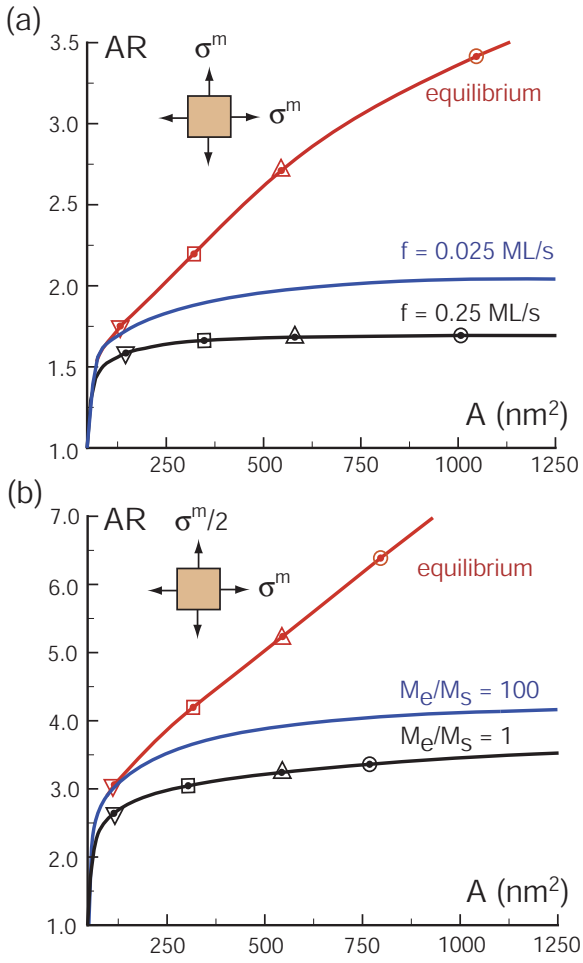

Figure 4.4: Aspect ratio (AR) vs. size (A) for (a) isotropic stress: $\sigma_{22}^m/\sigma_{11}^m = 1$ and (b) anisotropic stress: $\sigma_{22}^m/\sigma_{11}^m = 0.5$. The growth shapes in (a) are computed with $M_e/M_s = 1$, while in (b) are computed with $f = 0.25$ ML/s. The shapes corresponding to the marked symbols are shown in Fig. 4.3.

low-temperature growth conditions, slow kinetics of growth can result in the shapes that are different from the predicted equilibrium shapes, as we discuss next.

To understand how shapes fall out of equilibrium, we have computed the shapes *during* growth using the dynamic phase-field model. Fig. 4.3(a) and Fig. 4.3(b) show growth shapes for the case of equi-biaxial mismatch and anisotropic mismatch strain, respectively. The evolution of aspect ratio for these cases is shown in Fig. 4.4. It can be observed that equilibrium and growth shapes are similar for small sizes; however, the shapes of large islands during growth are much less elongated than the equilibrium shapes. In equilibrium, the widths of the islands are nearly independent of size. On the other hand, widths are observed to increase with size during growth. Hence, the aspect ratios during growth (refer to Fig. 4.4) increase initially before saturating at levels that are much lower than the corresponding equilibrium values. A similar increase in the width has recently been observed in case of epitaxial germanide islands on Ge(001) during deposition of Fe [Li *et al.* (2007)].

Next, we explain the reasons behind the large differences in the aspect ratios of islands close to and far from equilibrium. In the regions surrounding the 'tips' (i.e., the regions of large curvature), gradients in the chemical potential – and hence the driving force for diffusion towards island boundary – are always larger than in the regions of small curvatures. Therefore, according to classic Mullins-Sekerka kinetic instability in diffusion-mediated growth, regions with large curvatures are expected to grow faster than the regions of small curvatures [Mullins and Sekerka (1963)]. This would suggest that the aspect ratio during growth will be *higher* than the corresponding equilibrium value, in contrast to the observations reported here. This apparent discrepancy can be understood by considering the effect of strain, as the relaxation of strain favors elongated shapes with constant widths as noted earlier (refer Fig. 4.3). In order to achieve growth with near-constant widths, the flux of adatoms from the terrace

towards regions of small curvatures needs to be negligible in comparison with flux towards the tips of the islands. However, during low-temperature growth conditions considered here, the small adatom flux towards center of the boundary always results in a gradual increase in the width and therefore smaller aspect ratios as seen in Fig. 4.4.

The above argument suggests that if the adatoms attached to the boundary have greater opportunity to diffuse towards the tips, the resulting growth shapes will be closer to the corresponding equilibrium shapes. This is indeed what we observed when the rate of deposition is lowered by a factor 10 [refer Fig. 4.4(a)]. With slower growth, the effective flux from the terrace towards the island boundaries is reduced leading to elongated growth shapes with higher aspect ratios. The effect of the competition between diffusion on the terrace and along the boundary is also clearly evident in Fig. 4.4(b). Here we consider the evolution of the aspect ratio when the mobility along the boundary (M_e) is enhanced in comparison to the mobility on the terrace (M_s) by two orders of magnitude. As in the case of growth with low deposition flux [Fig. 4.4(a)], the aspect ratios in this case are closer to equilibrium values compared to the case when $M_e/M_s = 1$. Finally, our simulations show that for large sizes the aspect ratios saturate even when the mobility along the boundary is large, or when the deposition flux is small. Therefore, as strained wires grow in size, elongation to the degree predicted by equilibrium models may not be possible.

4.4 Monolayer islands on Si(001)

We next consider homoepitaxial growth of monolayer islands on Si(001) [Zielasek *et al.* (2001)] as an example of a material system where relaxation of anisotropic strain results in shapes that are characteristically different from the cases studied in the previous section. The dimer rows that run along the $\langle 110 \rangle$ directions of Si(001)

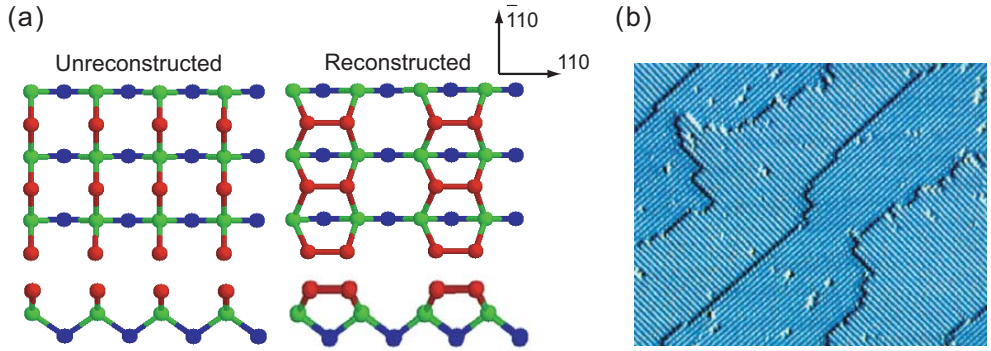

Figure 4.5: (2×1) surface reconstruction on Si(001). (a) A schematic, and (b) an STM image showing rotation of dimer rows by 90 °across a step [Zandvliet (2000)].

surface lead to a strong anisotropy in the surface stress tensor; the surface is under compressive stress along the dimer rows while it is under tensile stress in the direction perpendicular to dimer rows [Zandvliet (2000)]. Furthermore, as illustrated in Fig. 4.5, the orientation of the dimer rows on the monolayer-high islands on this surface is rotated by 90^o relative to the orientation of the dimer rows on the terrace below. Subsequently, the differences in the surface stress between the island and the terrace along the two $\langle 110 \rangle$ directions are equal but opposite in sign: $\sigma_{11}^m = -\sigma_{22}^m$ with $\sigma_{12}^m = 0$. Since the boundaries of the island are formed by alternating low-energy S_A and high-energy S_B steps that are oriented along $\langle 110 \rangle$ directions, the free energy of the island boundary is also anisotropic with a two-fold symmetry. However, to analyze the role of strain anisotropy in the shape evolution of islands, it is convenient to first consider a simple case where the boundary energy is assumed to be isotropic. Next, we consider the equilibrium shapes for this special case.

In order to determine the equilibrium shape, we start with a square-shaped island with its sides oriented along $\langle 110 \rangle$ directions and let it evolve in the absence of a flux (i.e., at a fixed size).[2] As shown in Fig. 4.6(a), we find that the island assumes a

[2]The governing equations for the dynamic growth model – described for the island strained due to the elastic mismatch with the substrate – are also valid for the homoepitaxially grown monolayer

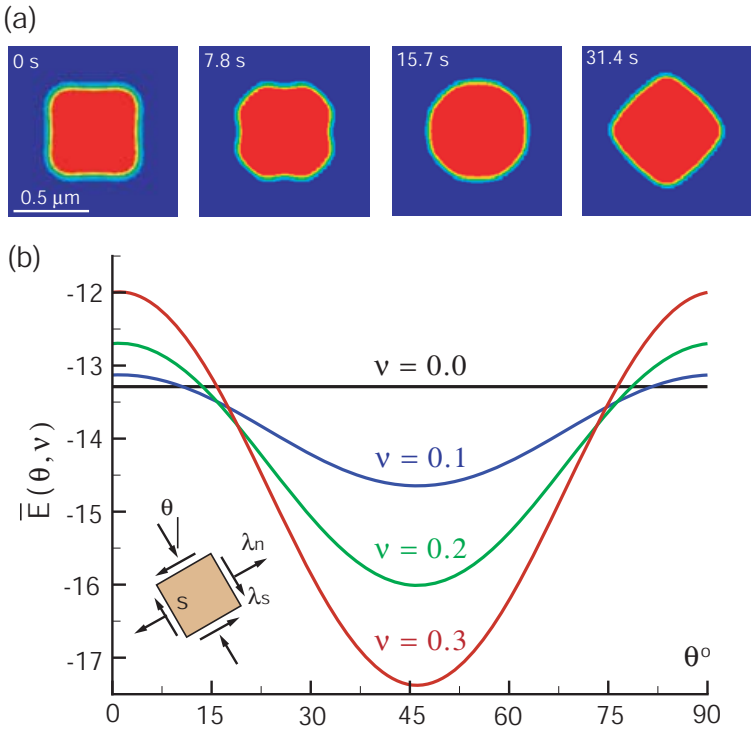

Figure 4.6: Effect of Poisson's ratio on the shapes of a monolayer island on Si(001). (a) Evolution towards the equilibrium shape for an island with isotropic boundary energy. (b) Normalized elastic energy $\bar{E}(\theta,\nu) = E_e/(\sigma^{m\,2}/\pi Y)$ of a square-shaped domain vs. orientation θ, plotted for $s = 0.5$ μm. The inset shows normal and shear components of force monopoles on the boundary of the island.

circular shape in the intermediate stages of evolution before finally equilibrating to a square shape with sides oriented approximately along the $\langle 100 \rangle$ directions. This suggests that elastic relaxation introduces a novel four-fold symmetry in the equilibrium shapes. As we explain next, the emergence of this symmetry can be explained by considering the orientation dependence of the elastic relaxation arising from a 'Poisson effect'.

The elastic relaxation energy of a monolayer island can be computed by considering the force monopoles arising from the discontinuity in surface stress at the

islands strained due to the discontinuity in surface stress at the island boundaries. In that case, $\sigma^m_{ij} h$ is the difference between the surface stress in the island and the surface stress in the terrace, with $W^m = 0$.

island boundaries. For a boundary orientation θ, the force monopoles have nonzero components acting normal to and along the boundary [refer to inset in Fig. 4.6(b)]. These normal (λ_n) and shear (λ_s) components of force monopoles are related to the orientation of the boundary θ as

$$\lambda_n = \sigma_{11}^m \cos(2\theta) \qquad \text{and} \qquad \lambda_s = -\sigma_{11}^m \sin(2\theta)\,. \tag{4.9}$$

The above expression shows that when island boundaries are oriented along $\langle 110 \rangle$ directions ($\theta = 0^o$), only normal forces act on the boundary, while for boundaries that are oriented along $\langle 100 \rangle$ directions ($\theta = 45^o$) force monopoles have only shear components.

In order to understand how the elastic relaxation favors boundaries oriented along $\langle 100 \rangle$ directions, consider the variation of elastic energy of a square-shaped island oriented at an angle θ as shown in of Fig. 4.6(b). For nonzero Poisson's ratio ν, the elastic energy is always minimum for $\theta \approx 45^o$. For $\nu = 0$, however, elastic energy is independent of the orientation. The reduction in elastic energy due to this Poisson's effect is significant – for $s = 0.5$ μm and a typical value of $\nu = 0.3$ for Si(001), the elastic energy is reduced by 45% when island boundaries are orienting along $\langle 100 \rangle$ directions compared to $\langle 110 \rangle$ directions. The observation that islands with sides along $\langle 100 \rangle$ are favored over all the other directions indicates that elastic relaxation arising from the shear component of the monopole is more efficient than the relaxation due to the normal component. This analysis clearly shows that the unique anisotropy in the surface stress on Si(001) gives rise to a novel 4-fold symmetry in equilibrium shapes – a symmetry that is not observed in other anisotropically strained systems.

In the case of the monolayer islands considered here, the relationship between the intrinsic length scale l^* in the phase field calculations and the elastic cutoff length δ in the sharp-interface models can be conveniently obtained by comparing the elastic

energy of square-shaped islands shown in Fig. 4.6. By computing elastic energy for domains of different sizes using surface elastic Green's functions [Landau and Lifshitz (1986)], we obtain the relation $l^* = 93.72\delta$. For a typical value of elastic cutoff $\delta = 0.15$ nm, we obtain l^*= 14 nm. For the surface diffusivity value used in the case of nanowires, we estimate the time scale as $t^* = 0.0392$ s. Next, we consider how the anisotropy in the boundary energy influences equilibrium and growth shapes of monolayer islands on Si(001).

The boundary energy of the monolayer islands on Si(001) is two-fold symmetric due to the anisotropy in the formation energies of S_A and S_B steps [Zandvliet (2000)]. Therefore, as in the case of nanowires, we use the parametric form for the boundary energy: $\beta(\theta) = \beta_0(1 - \alpha\cos(2\theta))$ where α is the temperature-dependent anisotropy factor. Figures 4.7(a) and 4.7(b) show the evolution of domain shapes and aspect ratios, respectively, for typical parameters $\alpha = 0.2$ and $F_0/\beta_0 = 0.27$. With these parameters, the aspect ratios of the domains obtained by our simulations are close to the aspect ratios observed in recent experimental observations of growth of stress domains on Si(001) [Zielasek *et al.* (2001)].

As in the case of nanowires, the shapes of small islands obtained during growth are similar to the equilibrium shapes [refer to Fig. 4.7]. However, the shape evolution of large islands on Si(001) is different in two aspects:

1. As the islands grow in size, the equilibrium aspect ratios are considerably smaller than the case of nanowires;

2. More importantly, in contrast to the case of nanowires, the aspect ratios during growth are *larger* than the corresponding equilibrium values.

Below, we discuss these aspects in detail starting with the equilibrium shapes.

The shapes of monolayer islands on Si(001) involve a competition between two effects – the anisotropy in the bond energies favors the formation of $\langle 110 \rangle$ oriented

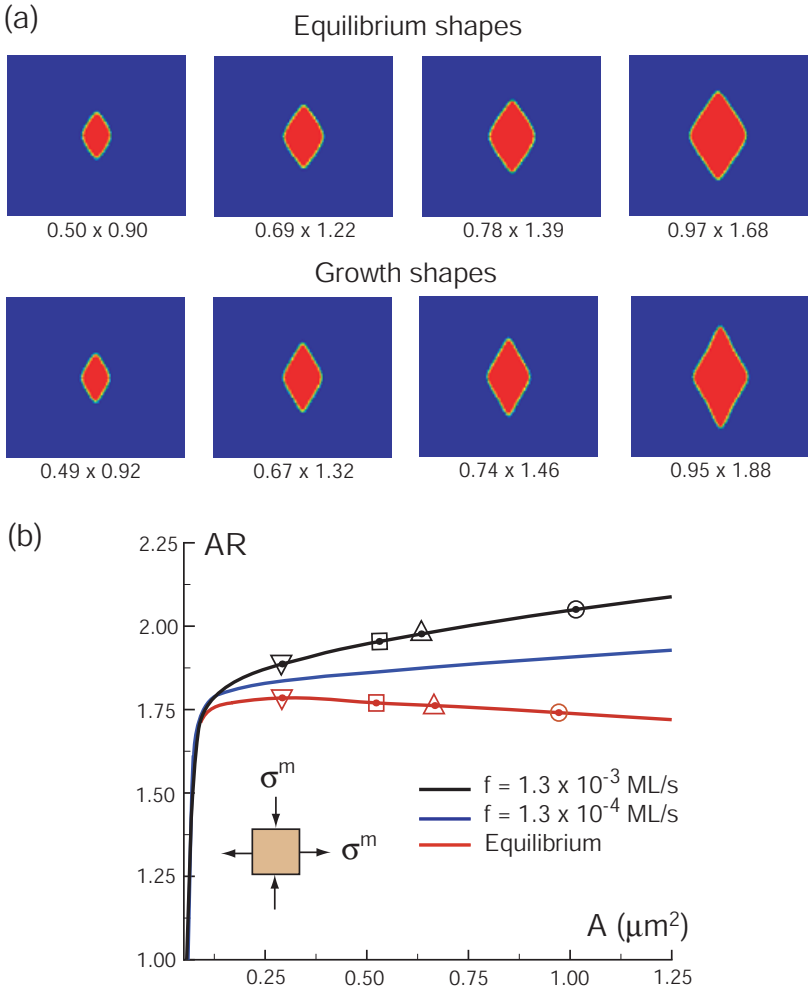

Figure 4.7: Shape evolution of a monolayer island on Si(001). (a) Equilibrium and growth shapes. The dimensions marking each shape represent the lengths of the minor and major axes in μm. (b) Evolution of the aspect ratio (AR) vs. size (A) during equilibrium and growth. The shapes corresponding to the marked symbols are shown in (a). The growth shapes are computed with $M_e/M_s = 1$.

boundaries, whereas the elastic relaxation is more favorable for boundaries oriented along $\langle 100 \rangle$ directions. The diamond-like equilibrium shapes of islands shown in Fig. 4.7(a) can therefore be understood as the squares (with sides along $\langle 100 \rangle$ directions) whose diagonals are stretched along the $\langle 110 \rangle$ directions due to the anisotropy in the boundary energy. Furthermore, we find that islands maintain a self-similar shape in equilibrium as they grow in size.

The observation of growth shapes whose aspect ratios are larger than the equilibrium shapes of similar sizes [Fig. 4.7(b)] can now be explained by invoking the curvature dependence of the growth speeds. In diffusion controlled growth, regions of high curvature tend to grow faster as the gradients in the chemical potentials are large in their vicinity [Mullins and Sekerka (1963)]. For a given flux, the tips along the long axis of the islands therefore grow at a faster rate leading to an increase in the aspect ratio of the island during growth. The effect of lowering the rate of deposition on growth shapes is similar to the previously studied cases – with slower growth, the aspect ratios are closer to the equilibrium values [refer Fig. 4.7(b)]. A similar behavior is observed when mobility of adatoms along the boundary (M_e) is increased in comparison to the mobility on the terrace (M_s). With increasing edge mobility, growth shapes are similar to the equilibrium shapes. In the experimental study on the shape evolution of monolayer islands on Si(001) [Zielasek *et al.* (2001)], the aspect ratios of islands were observed to increase with the size of the domain. Since our simulations show that the aspect ratio in equilibrium is nearly independent of size, the shapes of large islands observed in these experiments are very likely limited by kinetics.

4.5 Chapter summary

Our simulations show that the anisotropy in strain plays a crucial role in the shape evolution of strained 2D systems during diffusion-limited growth. Though

thermodynamics of anisotropic strain relaxation favors formation of highly elongated nanowires, the kinetics of diffusion-limited growth can in many cases result in shapes that are less elongated. Further, we have shown that the unique anisotropy in surface stress for domains on Si(001) gives rise to a 4-fold symmetry in the shapes. This surface stress-induced symmetry, coupled with kinetics of growth results in growth shapes that are more elongated than the equilibrium shapes. Finally, our study also provides a means to quantitatively determine various thermodynamic and kinetic material parameters (for example, boundary free energy and mobility of adatoms) by comparing the shapes observed under various growth conditions.

Chapter 5

Composition maps in self-assembled alloy quantum dots

5.1 Introduction

A particularly appealing approach to manufacturing nanoscale devices is to exploit the natural tendency of small material clusters to self-organize. While strain-driven self assembly can give rise to nanoscale pattern formation of 2D domains and islands as discussed in previous chapters (refer Chapters 2-4), it also provides a versatile means to fabricate nanoscale islands in lattice-mismatched semiconductor *alloy* systems which can serve as functional elements in optical, electronic and photo-voltaic devices [Heiss (2005), Wang (2007)]. The electronic structure of these nanoscale islands or 'quantum dots' is strongly influenced by the shape, elastic deformation and most importantly by their composition, thereby enabling the device properties to be controlled. A tighter control of these characteristics significantly reduces power consumption and heat generation, while the small dimensions of the devices allow order of magnitude advances in miniaturization. Self assembled SiGe [Medeiros-Ribeiro *et*

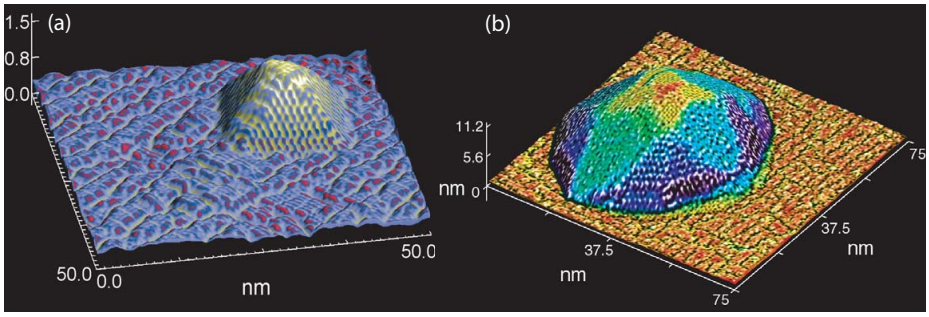

Figure 5.1: STM images of Ge quantum dots on Si(001): (a) Pyramid, and (b) Dome. Pyramid is bounded by {105} facets, while dome is bounded by {113} and {15 3 23} facets [Medeiros-Ribeiro *et al.* (1998)].

al. (1998), Drucker (2002)] (refer Fig. 5.1) and InGaAs [Stangl *et al.* (2004)] quantum dots have received particular attention as the former material system can be readily integrated with the well developed Si integrated circuit technology while the latter has been successfully applied in photovoltaic and photonic bandgap applications.

The past few years have seen tremendous advances in development of processing and patterning techniques that lead to a uniform array of quantum dots of nearly identical shapes and sizes [Gray *et al.* (2004), Grutzmacher *et al.* (2007)]. However, key factors that play a role in controlling the variations in composition within the quantum dots remain poorly understood. A quantitative determination of the composition profiles is critical in device applications as variations in composition at the nanoscale can substantially influence the electronic properties (for example, excitonic transitions [Shumway *et al.* (2001)], electron-hole band alignment and band gaps [Sheng and Leburton (2001)]) and therefore directly influence the performance of devices. While there is a large body of theoretical work on the formation and growth of quantum dots, almost all of it neglects alloying effects by assuming a uniform composition distribution within the dots.

In recent years, considerable progress has been made in measuring the composition profiles within individual quantum dots with nanoscale resolution [Floyd *et al.* (2003),

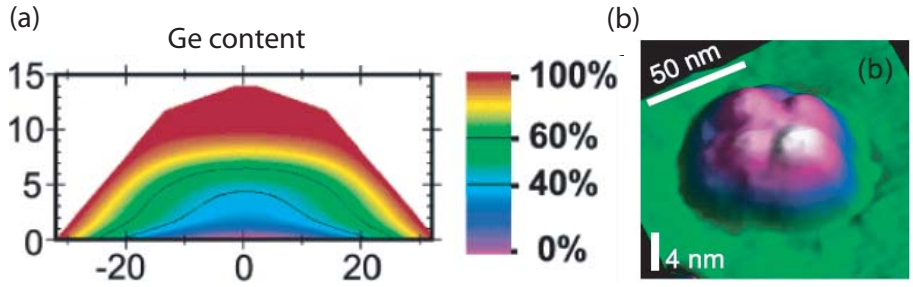

Figure 5.2: (a) Composition profiles in dome-shaped SiGe quantum dot obtained from x-ray scattering data [Malachias *et al.* (2003)]. The dimensions are in nm. (b) 3D AFM image showing rosette morphology of dome-shaped SiGe quantum dot after selective Ge etching [Leite *et al.* (2007)].

Malachias *et al.* (2003), Denker *et al.* (2003, 2005), Leite *et al.* (2007), Katsaros *et al.* (2005), Medeiros-Ribeiro and Williams (2007)]. These experimental studies show two distinct types of scenarios:

1. The work of Stanley Williams and coworkers using x-ray scattering and independent selective etching techniques [Malachias *et al.* (2003), Leite *et al.* (2007), Medeiros-Ribeiro and Williams (2007)] shows a Si-rich core covered by a Ge-rich shell (Fig. 5.2) for dome shaped SiGe quantum dots at 600 °C.

2. In distinct contrast, the work of Schmidt and coworkers using a combination of selective wet chemical etching and atomic force microscopy [Denker *et al.* (2003, 2005)] shows that for pyramid and dome shaped islands, the corners are highly intermixed, whereas the edges, apex and the center of the pyramids remain Ge rich at 550 °C.

Given the sensitivity of the composition profiles in the quantum dots to growth conditions and the differences between the experimental measurements from different groups, information from these experiments can only be properly interpreted with models that can distinguish the differences between composition profiles under different growth conditions. To that end, a key question that one is generally faced with

in these experiments is whether or not a measured profile is close to equilibrium.

In equilibrium, for a given size and shape of the dot, the composition profile is obtained by minimizing the total free energy that consists of the elastic energy and entropic and chemical mixing energies. The primary difficulty in obtaining composition profiles is that the shape, strain and composition are all coupled to each other. Furthermore, in equilibrium, the total free energy has to be minimized by holding the overall ratio of the alloy components in the dot at a fixed level, making the optimization problem even more difficult. Subsequently, only calculations that adopt a number of simplifying assumptions such as small slopes of the sidewalls of the quantum dots [Spencer and Blanariu (2005)] and linear extrapolation of the composition profiles from the surface to the bulk [Liu *et al.* (2000)] are available. The approximations made in the calculations allow only for the analysis of pre-pyramid clusters with very shallow side-walls. Monte Carlo methods have also been employed to analyze quasi-equilibrium composition profiles [Hadjisavvas and Kelires (2005), Lang *et al.* (2005)], but the long range nature of the elastic interactions makes statistical sampling of the large configuration space (required to obtain properly averaged composition maps in realistic structures) a very demanding and tedious task.

In this chapter, we study equilibrium composition maps in quantum dots by employing the finite element method for rigorous treatment of elastic fields without any restrictions on their shape and an optimization scheme based on quadratic programming methods. We find that the shapes of the quantum dots play a very important role in determining the degree of alloy decomposition that can be achieved at a given temperature. The composition profiles in faceted quantum dots with steep side-walls are found to be characteristically different from the corresponding case of shallow dots. In the former case, segregation of the larger alloy component in the tensile regions of the quantum dot leads to the formation of 'cusped' composition profiles

which manifest in the form of dimpled surface profiles upon selective etching of one of the alloy components (Fig. 5.4). Shallower islands on the other hand, are less decomposed and yield surface profiles with large etch pits. Both of these features have been observed during wet chemical etching of SiGe quantum dots [Malachias *et al.* (2003), Denker *et al.* (2003), Leite *et al.* (2007)].

In order to guide the interpretation of composition maps measured in experiments, the degree of alloy decomposition in faceted quantum dots is presented in a phase diagram plotted in the space spanned by the orientation of their side-walls and temperature. Based on this phase diagram, the effect of decomposition on the shape transition between quantum dots with different facet orientations is computed – alloy decomposition is found to significantly decrease the transition volumes for shape transformation. To further demonstrate the role of shape and strain on alloy decomposition at the nanoscale, we have considered the composition profiles of dome, truncated pyramid and unfaceted pre-pyramid or Gaussian shaped quantum dots, all of which have been observed in SiGe [Medeiros-Ribeiro *et al.* (1998), Ross *et al.* (1999), Vailionis *et al.* (2000), Costantini *et al.* (2005)] and InGaAs [Costantini *et al.* (2005), Kratzer *et al.* (2006)] systems. In the case of dome and truncated-pyramid shaped quantum dots with multiple facets, we find a rich array of compositional patterns with enrichment of the larger alloy component at the corners and edges formed by the intersection of different facets. In the case of unfaceted quantum dots, both the slopes and curvatures of the surface are found to influence compositional patterning.

This chapter is organized as follows. In Sec. 5.2, we briefly outline the mathematical model that quantitatively describes the competition between strain-induced segregation and thermodynamics of mixing in an alloy quantum dot. The equilibrium composition maps in simple cone-shaped dots obtained using this model are given in 5.3. In Sec. 5.4, we present a compositional phase diagram that shows the degree of

alloy segregation as a function of temperature and shape of the faceted dot, while the effect of alloy segregation on the critical size for the transition in shapes of faceted quantum dots is demonstrated in Sec. 5.5. In Sec. 5.6, we describes the composition profiles in various dome and pyramid shaped quantum dots that are observed in SiGe and InGaAs systems. Finally, the conclusions drawn from our analysis are summarized in Sec. 5.7.

5.2 Mathematical model for equilibrium composition maps in alloy quantum dots

For an AB alloy quantum dot grown epitaxially on a substrate of species A, the total free energy E of the quantum dot-substrate system can be written as $E = E_{ch} + E_{el} + E_s$, where E_{ch} is the chemical free energy of the alloy components in the quantum dot, E_{el} is the elastic strain energy due to the lattice mismatch between the quantum dot and the substrate, and E_s is the surface energy cost involved in the formation of the quantum dot. While elastic fields tend to favor segregation of the larger alloy component near more tensile regions in the dot, thermodynamic mixing free energy (which depends on temperature) can prevent the decomposition of the alloy. In equilibrium, for a given shape of the quantum dot, the composition profile is determined by a competition between these two contributions.

In general, the functional form of the thermodynamic mixing free energy of the alloy, which includes both enthalpic and entropic contributions, can be quite involved, although the latter contribution dominates at high temperatures, favoring complete mixing of the alloy components. In order to capture the key aspects of mixing effects,

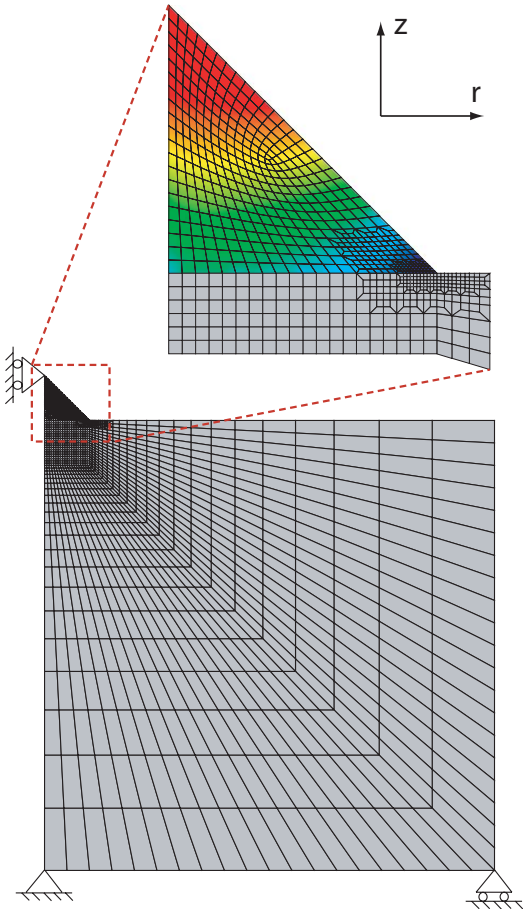

Figure 5.3: The finite element mesh used for the computation of the elastic fields for an axially symmetric quantum dot. The volume of the substrate used in the calculations is three orders of magnitude larger than the volume of the quantum dot, so that finite-size effects are negligible.

we write the chemical free energy of the alloy quantum dot as

$$E_{ch} = \int_{V_d} f(c)\, dV, \tag{5.1}$$

where V_d is the volume of the dot, $c(\mathbf{x})$ is the mole fraction (or composition) of the B-species in the alloy and the free energy density is taken to be $f(c) = \Delta F(T)\, c + F_m(T)\, c(1-c)$. Here, $\Delta F(T)$ is the free energy difference between the phases A and B and T is the temperature. The contribution to the total energy of the quantum

dot from the first term in $f(c)$ is $\Delta F(T)\bar{c}V_d$, where $\bar{c}$ is the average composition in the dot. If the average composition is maintained, this term is independent of the composition profile in the dot, $c(\mathbf{x})$, and therefore does not play a role in the determination of the equilibrium distribution of alloy components. On the other hand, the temperature dependent parameter $F_m(T)$ determines stability of the alloy to phase separation – for $F_m > 0$ alloy thermodynamics favors phase separation into A and B components, while $F_m < 0$ results in complete mixing of alloy components at any composition. In what follows, we will consider the composition profiles for both positive and negative values of F_m, representative of the thermodynamics of mixing at low and high temperatures, respectively.

The elastic energy of the quantum dot-substrate system can be written as

$$E_{el} = \frac{1}{2}\int_{V_d+V_s} C_{ijkl}(\epsilon^r_{ij} + \epsilon^0_{ij})(\epsilon^r_{kl} + \epsilon^0_{kl})\, dV\,, \tag{5.2}$$

where ϵ^r_{ij} is the relaxation strain and $\epsilon^0_{ij} = \epsilon_m c(\mathbf{x})\delta_{ij}$ is the composition-dependent mismatch strain in the quantum dot, ϵ_m being the equi-biaxial mismatch strain arising due to the difference in the lattice constants between species A and B. In our calculations, the quantum dot and the substrate are assumed to be isotropic linear elastic materials with identical elastic constants C_{ijkl}.

For a given shape and size of the quantum dot, the equilibrium composition profiles are determined by minimizing the sum of the chemical (Eq. 5.1) and elastic (Eq. 5.2) energies with respect to local composition $c(\mathbf{x})$. The elastic fields arising from variations in the local composition are computed using finite element methods (Fig. 5.3) and the total energy of the quantum dot is optimized using a sequential quadratic programming method [Schittkowski (1986)]. A combination of these techniques allows us to determine the equilibrium composition profiles for any shape, without invoking any approximations in computing the elastic fields.

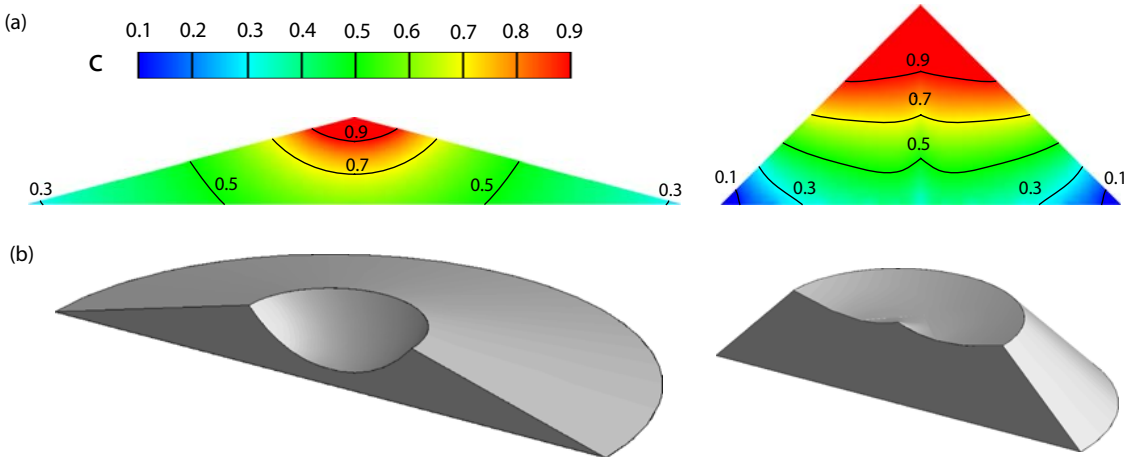

Figure 5.4: Influence of morphology on the equilibrium composition profiles in alloy quantum dots. (a) Composition profiles in axially symmetric quantum dots of identical size, but with shallow (left) and steep side-walls (right). The steeper side-walls allow for larger strain relaxation resulting in a greater degree of segregation of alloy components at the apex and in the periphery of the dots. The composition profiles are obtained for $F_0 = -0.2$ and with average composition $\bar{c} = 0.5$. (b) The 3D rendering of the shapes of the quantum dots in (a) upon etching with a selective chemical agent that dissolves regions of dot whose composition, c, exceeds 65%. The segregation indices (Eq. 5.4) for the steep and shallow dots are 0.177 and 0.051, respectively.

5.3 *Composition maps in a cone-shaped quantum dot*

The role of shape on the distribution of the alloy components is first considered for the case of cone-shaped quantum dots shown in Fig. 5.4. The composition profiles in these dots depend only on three parameters, namely, the average composition $\bar{c}$, the sidewall angle θ and the ratio of the chemical and elastic energy densities, $F_0 = F_m/(M\epsilon_m^2)$, where M is the biaxial modulus. This observation follows from the fact that the chemical and the elastic energies (Eqs. 5.1 and 5.2) scale linearly with the volume of the quantum dot, which allows us to write their sum in the form

$$E_{ch} + E_{el} = M\epsilon_m^2 V_d \, \hat{W}(\bar{c}, \theta, F_0), \tag{5.3}$$

where $\hat{W}$ is a dimensionless function. Since this function does not depend on size, the equilibrium composition profile in a 'faceted' quantum dot with a given sidewall angle θ is independent of its volume, V_d.

The equilibrium composition profiles in 50-50 alloy quantum dots with sidewall angles of 15°and 45°are shown in Fig. 5.4(a). Here, we have taken $F_m = -0.2\, M\epsilon_m^2$, so that alloy thermodynamics favors complete mixing. However, strain leads to segregation of the larger alloy component (B) at the apex while the corners of the dot near the substrate are enriched in the other component (A). The degree of decomposition depends on the shape – segregation of the alloy components at the apex and at the periphery is much larger in the steeper dot. The 50% isocomposition profile in this case is located nearly half way between the substrate and the apex of the dot, while this profile in the shallower case lies between the axis of symmetry and the periphery of the dot. Furthermore, the isocomposition profiles that lie above the substrate in the steeper dot develop a 'cusp' at the axis of symmetry. This feature, which is absent in the shallower dot, should be observed by etching the structures with a selective chemical agent that removes material above a threshold level of composition. The 65% isocomposition surface profiles given in Fig. 5.4(b) for the two cases show very distinct shapes – the steeper dot develops a nearly flat top with a 'dimple' along its symmetry axis, whereas a deep pit is formed in the shallower dot. Similar features of etched surfaces have been observed in dome and pyramid shapes SiGe quantum dots, respectively [Malachias *et al.* (2003), Denker *et al.* (2003), Leite *et al.* (2007), Katsaros *et al.* (2005)]. However, kinetic effects, for example, the smaller diffusion length of Ge compared to Si, can also possibly give similar shapes upon selective etching [Katsaros *et al.* (2005)]. Further experiments that consider the surface profile as a function of annealing time are needed to determine if the measurements correspond to equilibrium predictions.

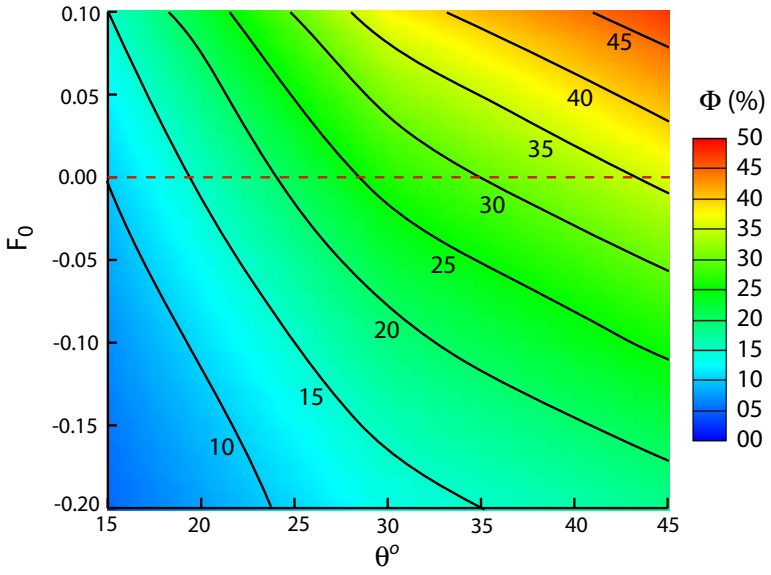

Figure 5.5: Compositional phase diagram showing degree of segregation, Φ as a function of the parameter F_0 and the shape of the quantum dot represented by the angle of side-walls, θ. Even when the thermodynamic mixing energy favors mixing ($F_0 < 0$), the relaxation of strain for quantum dots with steep side-walls results in the alloy segregation within the quantum dot. Similarly, when thermodynamics favors phase separation ($F_0 > 0$), complete decomposition is not observed. The average composition $\overline{c}$ of the quantum dot is 0.5.

5.4 Compositional phase diagram

Strain-induced alloy segregation in the quantum dots can be analyzed in a quantitative manner by considering the segregation index Φ, which we define as

$$\Phi(F_0, \theta) = \frac{4}{V_d} \int_{V_d} (c(\mathbf{x}) - \overline{c})^2 \, dV \, . \tag{5.4}$$

For a 50-50 alloy quantum dot, the alloy components are completely mixed (i.e. $c(\mathbf{x}) = 0.5$ everywhere) when $\Phi = 0$, while $\Phi = 1$ corresponds to complete alloy decomposition. The computed level curves of the segregation index are plotted in Fig. 5.5 as a function of the ratio F_0 and the facet angle, θ and segregation indices for InGaS and SiGe quantum dots at typical growth temperatures are given in Table 5.1.

	InGaAs/GaAs			SiGe/Si		
T	$M\epsilon_m^2$	F_m	$\Phi(30°)$	$M\epsilon_m^2$	F_m	$\Phi(30°)$
400 °C	4.86	-0.80	0.151	2.82	-3.00	0.021
600 °C	4.86	-1.91	0.075	2.82	-4.90	0.010

Table 5.1: Segregation index for InGaAs/GaAs and SiGe/Si quantum dots with side-wall angles of 30°. The strain energy density, $M\epsilon_m^2$ and the coefficient of the mixing energy F_m are in given units of 10^8Joules/m^3. The coefficient $F_m(T)$ is obtained by fitting $f(c)$ to the mixing energy density, $\Omega c(1-c) + (k_BT/v_a)\,[c\log c + (1-c)\log(1-c)]$, where the regular solution interaction parameter Ω is taken to be 3.47 and 4.12 $\times 10^8$ Joules/m^3 for SiGe/Si and InGaAs/GaAs, respectively [Spencer and Blanariu (2005)] and v_a is the atomic volume. The table shows that the degree of decomposition is considerably greater in InGaAs quantum dots compared to SiGe dots at typical growth temperatures.

As anticipated, the segregation index increases with increasing θ, but complete segregation of the alloy components is not achieved even when alloy thermodynamics favors phase separation ($F_0 > 0$). Similarly, complete mixing is only seen for very shallow dots when F_0 is sufficiently negative.

To understand why complete segregation is not observed when thermodynamics favors alloy decomposition ($F_0 > 0$), we consider the elastic energy of a nominally flat

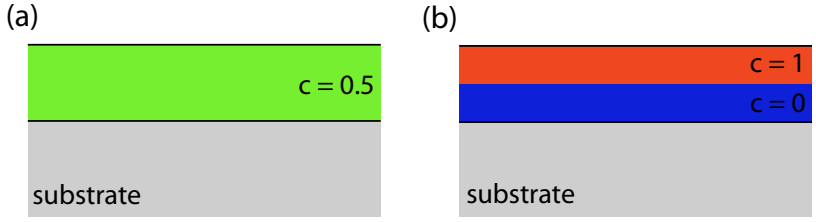

Figure 5.6: Schematic of an epitaxial lattice mismatched film of uniform thickness with (a) uniform composition ($c = 0.5$) and (b) complete alloy decomposition into individual components. Elastic energy is lower for the former configuration due to quadratic scaling of the strain energy density with the composition dependent mismatch strain, $c\epsilon_m$.

50-50 alloy film in two extreme cases: a) when the composition in the film is uniform and b) the film is completely phase separated (refer to Fig. 5.6). In the former case, the elastic energy per unit volume of the film is $M\epsilon_m^2/4$, while in the latter case it is $M\epsilon_m^2/2$. Clearly, because of the quadratic scaling of the strain energy density with the composition dependent mismatch strain, $c\epsilon_m$, a completely mixed alloy film has lower elastic energy than a phase separated film. Therefore, in the absence of in-plane strain relaxation, the elastic contribution to the total free energy always favors uniform composition even when alloy thermodynamics favors decomposition. Phase separation cannot occur unless the energetic gain from thermodynamics is sufficiently large, or when the condition $F_m > M\epsilon_m^2$ is satisfied. Extending this argument to the case of quantum dots whose shapes allow for strain relaxation, one can see that complete phase separation can only be achieved when the parameter, F_0 is sufficiently large.

5.5 *Critical size for shape transition in quantum dots*

Next, we show that strain-induced segregation in quantum dots can substantially reduce the critical size for transition between the shapes with different facets [refer Fig. 5.1(a)]. It is well known that with increasing size, shallow SiGe and InGaAs dots transform to steeper domes [Medeiros-Ribeiro *et al.* (1998), Ross *et al.* (1999), Vailionis *et al.* (2000), Costantini *et al.* (2005), Kratzer *et al.* (2006)], as strain can be more efficiently relaxed in the latter case. The critical volume for shape transition depends on the surface energies of the facets and the nominally flat film, which, in general, can all be different from each other. However, the key features of this transition can be studied by assuming that all the surface energies involved are equal.

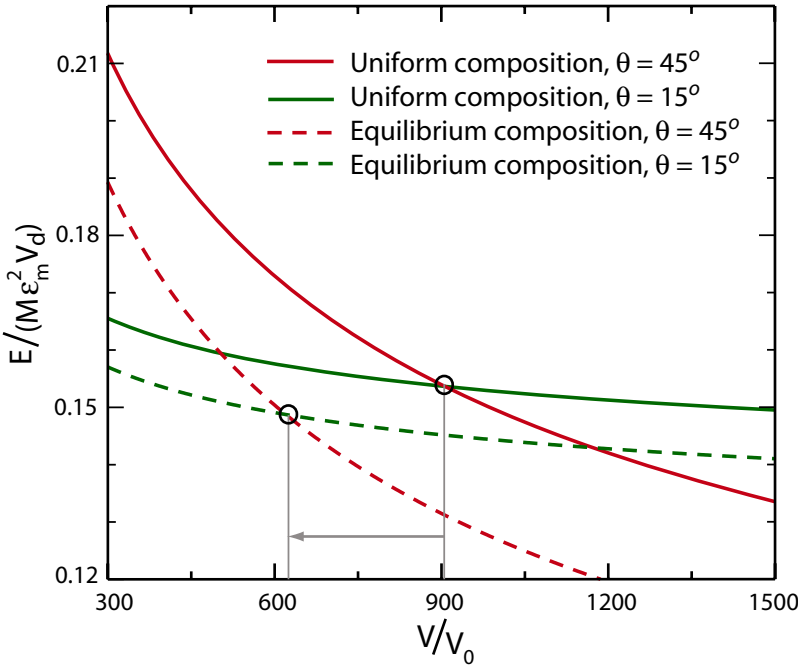

Figure 5.7: Variation of the energy per unit volume for quantum dots with shallow and steep side-walls ($\theta = 15°$and $\theta = 45°$, respectively) as a function of their size (normalized by the characteristic volume, $V_0 = [\gamma/(M\epsilon_m^2)]^3$. The total energy of the decomposed dots (dotted lines) is lower than the energy of dots with uniform composition, $\overline{c} = 0.5$ (bold lines). However, the reduction in the energy is greater for the steeper dot, resulting in smaller critical size for transition in shape. The surface energies for shallow and steep side-walls are assumed to be identical and the mixing parameter $F_0 = -0.2$.

In this case, for dots with uniform composition, shape transitions occur at a size when the gain in the elastic energy obtained by the formation of the steeper dots offsets the cost of forming the sidewall surfaces. However, if the decomposition of the alloy is permitted, one can see that steeper dots allow for even larger reduction of the elastic energy as the alloy components can redistribute themselves more readily to strain-relaxed regions (Fig. 5.4). Using the dimensionless function $\hat{W}$ (Eq. 5.3) obtained from our optimization procedure, the total energy of an alloy dot can then be expressed as

$$E = M\epsilon_m^2 V_d \, \hat{W}(\overline{c}, \theta, F_0) + \gamma \, V_d^{2/3} \hat{\Gamma}(\theta) \,, \tag{5.5}$$

where the surface energy, γ, is assumed to be independent of the facet angle, θ and

$$\hat{\Gamma}(\theta) = \pi\left(\frac{3}{\pi\tan(\theta)}\right)^{2/3}\left(\sqrt{1+\tan^2(\theta)}-1\right). \tag{5.6}$$

A plot of the energy per unit volume of decomposed dots in Fig. 5.7 (for $F_0 = -0.2$) shows that the volume to transition from a sidewall angle of 15° to 45° reduces by nearly 30% relative to the transformation volume of the dots with uniform composition.

5.6 Composition maps in faceted and pre-pyramid quantum dots

In equilibrium, SiGe and InGaAs quantum dots can also adopt shapes that consists of two or more facet orientations [Medeiros-Ribeiro *et al.* (1998), Ross *et al.* (1999), Vailionis *et al.* (2000), Costantini *et al.* (2005), Kratzer *et al.* (2006)]. The computed equilibrium composition maps in such dome and truncated-pyramid shaped quantum dots are shown in Fig. 5.8. A distinguishing feature of these dots is the intricate pattern of isocomposition profiles that can be attributed to the presence of 'corners' formed by the intersection of different facets. Since such corners allow for relaxation of mismatch strain, the free energy can be lowered by segregation of the larger alloy component in these regions. The number of extrema in the composition maps can therefore be directly correlated to the occurrences of facet intersections in the dot shape. The composition profiles in the regions close to the periphery of the base, however, are similar to the corresponding profiles in conical dots in Fig. 5.4.

Finally, we consider the equilibrium composition profiles in Gaussian 'pre-pyramid' quantum dots whose mean curvature varies in a non-monotonous manner from the apex to the base. The composition maps in two such dots of identical size but

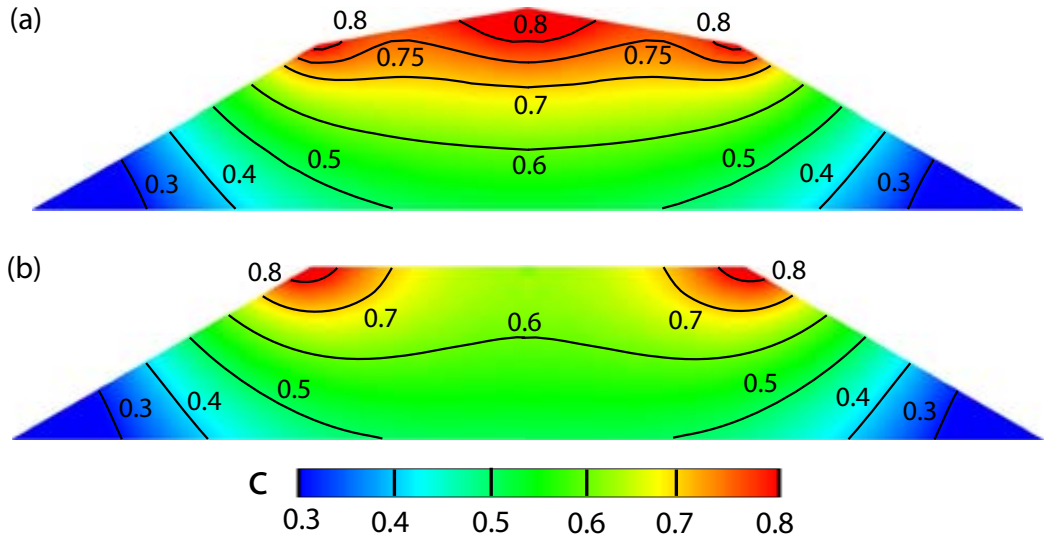

Figure 5.8: Equilibrium composition profiles in axially symmetric quantum dots with (a) 'dome' shape, the angles of the side-walls being 30^o and 15^o, and (b) a truncated-cone shape with a sidewall angle of 30^o. While the composition profiles are similar near the base, larger strain relaxation in the regions near the corners results in a greater segregation in the apex of the dome-shaped quantum dot. The composition profiles are obtained for $F_0 = -0.2$ and the average composition $\bar{c}$ is 0.5.

with different aspect ratios (the ratio of the height to the base width) are shown in Fig. 5.9. In both cases, the larger alloy component (B) segregates in the convex regions near the apex where the lateral strain is tensile, while the smaller alloy component segregates in the concave regions near the periphery of the dot. As in the case of the faceted islands (Fig. 5.4), the degree of decomposition is greater in the steeper dot as evidenced by the location of the 50% isocomposition line – for the steeper dot it is located above the substrate, whereas it is closer to the axis of symmetry in the case of the shallower dot. While the composition profiles in the shallow dot [Fig. 5.9(a)] are qualitatively similar to the profiles obtained by assuming small surface slopes [Spencer and Blanariu (2005)], the advantages of our approach are evident from the characteristically different composition profiles for steeper Gaussian dots [Fig. 5.9(b)] and also from the profiles in the dots with complex shapes such as the dome and the

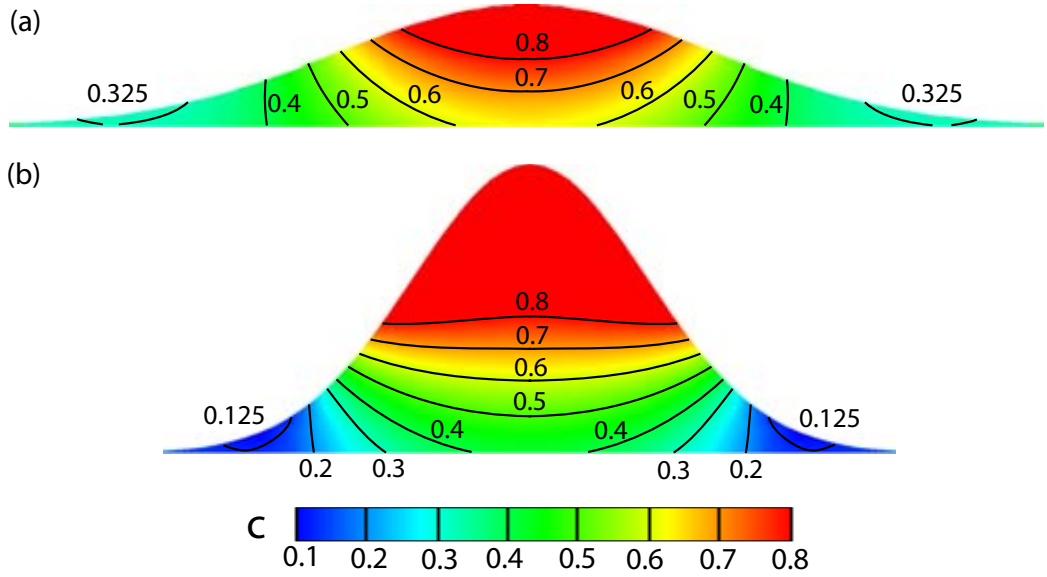

Figure 5.9: Equilibrium composition profiles in axially symmetric Gaussian pre-pyramid quantum dot (a) with aspect ratio (ratio of the height to width) of 0.12, and (b) with larger aspect ratio of 0.39. In the shape with smaller aspect ratio (part a), the regions near the base are considerably mixed, while the central region forming the core is rich in species B. Due to greater strain relaxation in the shape with larger aspect ratio (part b), species B segregates largely near the apex leaving the core regions near the base rich in species A. The composition profiles are obtained for $F_0 = -0.2$ and the average composition $\bar{c}$ is 0.5.

truncated-cone (Fig. 5.8).

5.7 *Chapter summary*

In summary, we have developed an efficient method to compute composition maps in strained alloy quantum dots and have shown that the composition profiles depend strongly on the slopes and curvatures of the surfaces of the dots as well as the presence of other geometric features such as corners and edges. Our approach provides a means to rigorously study the interdependence of the shape, strain and composition in lattice mismatched systems. The method can therefore be employed to analyze

compositional patterning in small scale structures such as nanowires [Owen *et al.* (2006)], nanorings [Sormunen *et al.* (2005)], nanotrees [Dick *et al.* (2006)], quantum fortresses [Gray *et al.* (2002)], quantum posts [He *et al.* (2007)] and quantum dot molecules [Gray *et al.* (2004)]. The next step in the analysis of such structures is to extend our method to include the dynamics of compositional patterns under non-equilibrium growth conditions. If the composition maps obtained using this approach are coupled with electronic structure calculations, a complete *in silico* characterization of the devices from growth to final performance can be achieved.

Chapter 6

Concluding remarks

It is well known that long-range elastic interactions can induce spontaneous formation of periodic patterns of 2D domains, nanowires and quantum dots. In many cases, the features have nanoscale dimensions, making them of interest for surface templating in non-lithographic, bottom-up fabrication of nanoelectronic devices. Therefore, a fundamental understanding of mechanics, thermodynamics and kinetics of self-assembly is necessary for reliable fabrication of ordered patterns of nanostructures envisioned for future nanoelectronics applications. Furthermore, since the characteristic features of the strain-induced self-assembled patterns can be directly related to key surface thermodynamic and kinetic parameters, detailed experimental investigations of the patterns also allow for a quantitative determination of these parameters.

In the work presented in this thesis, using a combination of experimental observations and predictions of mathematical models, we have shown that coupling between long-range elastic interactions, surface thermodynamics and kinetics of material transport gives rise to a wide range of novel morphological and compositional patterns in 2D self-assembling systems and quantum dots. Furthermore, since the functional form of elastic interactions is similar to magnetic or electrostatic interactions, our work is of generic nature and therefore should find broad applicability in a variety

of self-assembling systems. The following section briefly summarizes the conclusions drawn from our studies.

6.1 Summary

Using real-time low-energy electron microscopy to observe the growth and shape evolution of self-assembled stress domains on Si(111) surfaces, we have shown that elastic strain leads to dramatic transformations in the shapes of large domains that are not predicted by existing theoretical models. By comparing the experimental observations on the formation of the stress domains with dynamic growth simulations, we have developed a quantitative understanding of how a self-assembling system falls out of equilibrium. Our work shows the non-equilibrium shapes that a domain adopts during growth depend very strongly on the azimuthal dependence of its boundary energy. Further, we have demonstrated that these 2D self-assembled domains can remain trapped in a large variety of long-lived and metastable shapes that arise from an interplay of crystalline anisotropy and relaxation of elastic strain. On commonly used cubic (111) substrates, these shapes include extended or stacked structures made up of triangular domains connected at their corners, compact shapes with both convex and concave curvatures and others with narrow and elongated arms. All of these distinct experimentally observed shapes can be explained within a unified framework based on a phase diagram that systematically classifies the metastable shapes as a function of their size.

While the surface stress in 2D domains discussed above is essentially isotropic, we have also analyzed the evolution of equilibrium and growth shapes of anisotropically strained 2D self-assembled structures using a dynamic growth model. As examples of such structures, we have studied the shapes of nanowires grown heteroepitaxially on cubic (001) surfaces and monolayer islands or stress domains grown homoepitaxially

on Si(001) surface. In the former case, the anisotropy in the mismatch strain in two principal directions is large, while in the latter case, the principal components of the strain are equal in magnitude and opposite in sign. In the case of nanowires, we find that slow kinetics of growth limits the formation of wire-like shapes with constant widths as predicted by equilibrium models. In particular, the aspect ratios of nanowires during growth are smaller than the equilibrium aspect ratios. For monolayer islands on Si(001), the anisotropy in strain gives rise to a novel 4-fold symmetry in their equilibrium shapes. This strain-induced symmetry, coupled with kinetics of growth can result in rich shape dynamics of monolayer islands on Si(001) as seen in recent experiments.

In the case of self-assembled alloy quantum dots, nanoscale variations in composition arising from the competition between chemical mixing effects and elastic relaxation can substantially influence their electronic and optical properties. Using a combination of finite element and quadratic programming optimization methods, we have developed an efficient technique to compute the equilibrium composition profiles in strained quantum dots. We have shown that the composition profiles depend strongly on the morphological features such as the slopes and curvatures of their surfaces and the presence of corners and edges as well as the ratio of the strain and chemical mixing energy densities. More generally, our approach provides a means to quantitatively model the interplay between the composition variations, temperature, strain and the shapes of small-scale lattice-mismatched structures.

The work presented in this thesis can be further extended to addresses a few outstanding issues related to strain-induced self assembly in *alloyed* 2D systems and quantum dots. In the following section, we briefly discuss some of these issues that can be handled within the analytical and computational methods developed here. The list of the topics discussed below, however, is by no means complete and is merely an

indication of the richness of the possible opportunities in this area.

6.2 Future outlook

6.2.1 Alloying in 2D self-assembling systems

While strain-driven self-assembly is widely viewed as a promising technique for nanoscale patterning 2D systems such as domains and nanowires, a reliable means to engineer the characteristic length scales that the patterns adopt during self-assembly is essential for nanoelectronics applications. Alloying with Ge provides a straightforward and direct means to achieve control over feature sizes of self-assembled structures. As it is demonstrated in case of SiGe quantum dots, Ge has an advantage of cost competitiveness as it can be effectively integrated with existing Si fabrication techniques [Singh *et al.* (2005)].

The continuum models for unalloyed 2D domains developed in this work (refer Chapters 2-4) can be further enhanced to include the effects of alloying with Ge. The strain in alloyed 2D systems will be dependent on local composition and therefore will vary within the structures. As shown in our work on the composition maps in alloy quantum dots (Chapter 5), the strain variations will lead to segregation of alloy components, thus influencing the shape of individual domains and their distribution in a large array of patterns. Further, we have shown that an interplay between strain and crystalline anisotropy can lead to the existence of metastable shapes which makes it difficult to achieve a regular array of domains of consistent size and shape (refer Chapter 3). As Ge alloying changes the local thermodynamics, in particular, surface stress and domain boundary energy, alloying with Ge can provide an effective means to transform the shapes trapped in local, metastable states. Finally, more complex and rich kinetic effects, such as significantly different transport properties

of alloy components, can also be included in modeling the non-equilibrium growth of alloyed 2D self-assembling systems. Comparison of the predictions of the model with real-time shape and composition profiles from the experimental work can provide a fundamental understanding of nanoscale patterning of alloyed 2D self-assembling systems.

6.2.2 Composition maps in fully-faceted and dislocated quantum dots

We have shown that when there are many facet orientations that an alloy quantum dot can adopt, the transition between shapes with different facets depends on both the size and composition in the quantum dot (refer Chapter 5). Building upon this idea, morphological phase diagrams that elucidate the shapes that the faceted quantum dots adapt (such as pyramids, huts and domes) as a function of their size and overall composition can be developed to study the effect of alloy segregation on the shape transition. Since these transformation volumes can be measured in experiments, the predictions of these calculations can be tested and therefore should be able to determine whether a measured composition profile is close to thermodynamic equilibrium.

It is well known that for large SiGe and InGaAs quantum dots (base width typically greater than 100 nm for SiGe dots [Drucker (2002)]), elastic energy is lowered through the formation of dislocations. Since dislocations produce their own characteristic strain fields, they can significantly influence the strain distribution in the dot and thereby their composition profiles [Hegadekatte *et al.* (2008)]. Furthermore, as the driving force for the motion of a dislocation depends on local strain, its shape and location is inherently coupled to the composition profiles in the dot. This coupled problem can be effectively treated by combining the optimization method developed

in our work to compute the composition profiles with dislocation dynamics [Shenoy *et al.* (2000)]. These computations will allow for a quantitative analysis of the composition profiles in dislocated quantum dots obtained recently using x-ray scattering [Liao *et al.* (2000)] and etching measurements [Merdzhanova *et al.* (2006)].

Bibliography

Alerhand, O. L., Vanderbilt, D., Meade, R. D. and Joannopoulos, J. D. (1988), 'Spontaneous formation of stress domains on crystal surfaces', *Physical Review Letters* **61**(17), 1973–1976. 2.1

Bimberg, D., Grundman, M. and Ledenstov, N. N. (1993), 'Quantum dots: a review', *Physics Reports* **243**, 73–167. 1

Brongersma, S. H., Castell, M. R., Perovic, D. D. and Zinke-Allmang, M. (1998), 'Stress-induced shape transition of $CoSi_2$ clusters on Si(100)', *Physical Review Letters* **80**(17), 3795–3798. 2.1, 1, 3.1, 3.4

Cahn, J. (1961), 'On spinodal decomposition', *Acta Metallurgica* **9**(9), 795–801. 4.2.1

Chen, Y., Ohlberg, D. A. A. and Williams, R. S. (2002), 'Nanowires of four epitaxial hexagonal silicides grown on Si(001)', *Journal of Applied Physics* **91**(5), 3213–3218. (document), 1.1, 1, 4.1, 4.1, 4.3

Costantini, G., Rastelli, A., Manzano, C., Acosta-Diaz, P., Katsaros, G., Songmuang, R., Schmidt, O. G., Von Kanel, H. and Kern, K. (2005), 'Pyramids and domes in the InAs/GaAs(001) and Ge/Si(001) systems', *Journal of Crystal Growth* **278**(1-4), 38–45. 5.1, 5.5, 5.6

Datta, S. (2005), *Quantum transport: Atom to transistor*, 1 edn, Cambridge University Press. 1

Denker, U. Rastelli, A., Stoffel, M., Tersoff, J., Katsaros, G., Costantini, G., Kern, K., Jin-Phillipp, N. Y., Jesson, D. E. and Schmidt, O. G. (2005), 'Lateral motion of SiGe islands driven by surface-mediated alloying', *Physical Review Letters* **94**(21), 4. 5.1, 2

Denker, U., Stoffel, M. and Schmidt, O. G. (2003), 'Probing the lateral composition profile of self-assembled islands', *Physical Review Letters* **90**(19), 4. 5.1, 2, 5.1, 5.3

Dick, K. A., Deppert, K., Karlsson, L. S., Seifert, W., Wallenberg, L. R. and Samuelson, L. (2006), 'Position-controlled interconnected InAs nanowire networks', *Nano Letters* **6**(12), 2842–2847. 5.7

Drucker, J. (2002), 'Self-assembling Ge(Si)/Si(100) quantum dots', *IEEE Journal of Quantum Electronics* **38**(8), 975–987. 1, 4.1, 5.1, 6.2.2

Eggleston, J. J., McFadden, G. B. and Voorhees, P. W. (2001), 'A phase-field model for highly anisotropic interfacial energy', *Physica D* **150**(1-2), 91–103. 2.5.1, 2.5.1, 2.5.1, 4.2.1, 4.2.1

Evans, M. M. R. and Nogami, J. (1999), 'Indium and gallium on Si(001): A closer look at the parallel dimer structure', *Physical Review B* **59**(11), 7644–7648. 1, 4.1

Floyd, M., Zhang, Y. T., Driver, K. P., Drucker, J., Crozier, P. A. and Smith, D. J. (2003), 'Nanometer-scale composition measurements of Ge/Si(100) islands', *Applied Physics Letters* **82**(9), 1473–1475. 5.1

Freund, L. B. and Suresh, S. (2003), *Thin film materials*, 1 edn, Cambridge University Press. 1

Gangopadhyay, S. and Nag, B. R. (1997), 'Energy levels in three-dimensional quantum-confinement structures', *Nanotechnology* **8**(1), 14–17. 4.1

Gray, J. L., Atha, S., Hull, R. and Floro, J. A. (2004), 'Hierarchical self-assembly of epitaxial semiconductor nanostructures', *Nano Letters* **4**(12), 2447–2450. 5.1, 5.7

Gray, J. L., Hull, R. and Floro, J. A. (2002), 'Control of surface morphology through variation of growth rate in SiGe/Si(100) epitaxial films: Nucleation of "quantum fortresses"', *Applied Physics Letters* **81**(13), 2445–2447. 5.7

Grutter, P. and Durig, U. (1995), 'Quasidendritic growth of Co induced by localized reconstruction of Pt(111)', *Surface Science* **337**(1-2), 147–152. (document), 2.6.1, 3.1, 3.1, 3.2, 3.3

Grutzmacher, D., Fromherz, T., Dais, C., Stangl, J., Muller, E., Ekinci, Y., Solak, H. H., Sigg, H., Lechner, R. T., Wintersberger, E., Birner, S., Holy, V. and Bauer, G. (2007), 'Three-dimensional Si/Ge quantum dot crystals', *Nano Letters* **7**(10), 3150–3156. 5.1

Hadjisavvas, G. and Kelires, P. C. (2005), 'Critical aspects of alloying and stress relaxation in Ge/Si(100) islands', *Physical Review B* **72**(7), 4. 5.1

Hannon, J. B., Heringdorf, F., Tersoff, J. and Tromp, R. M. (2001), 'Phase coexistence during surface phase transitions', *Physical Review Letters* **86**(21), 4871–4874. 2.2

Hannon, J. B., Hibino, H., Bartelt, N. C., Swartzentruber, B. S., Ogino, T. and Kellogg, G. L. (2000), 'Dynamics of the silicon (111) surface phase transition', *Nature* **405**(6786), 552–554. 2.5.1, 2.5.2

Hannon, J. B., Tersoff, J. and Tromp, R. M. (2002), 'Surf ace stress and thermodynamic nanoscale size selection', *Science* **295**(5553), 299–301. (document), 1.1, 1, 2.1, 2.1, 2.2, 2.5.2, 3.2, 3.3, 4.1

He, J., Krenner, H. J., Pryor, C., Zhang, J. P., Wu, Y., Allen, D. G., Morris, C. M., Sherwin, M. S. and Petroff, P. M. (2007), 'Growth, structural, and optical properties of self-assembled (In,Ga)As quantum posts on GaAs', *Nano Letters* **7**(3), 802–806. 5.7

Hegadekatte, V., Medhekar, N. V. and Shenoy, V. B. (2008), 'Composition maps in dislocated alloy quantum dots', *In preparation*. 6.2.2

Heiss, W. D. (2005), *Quantum Dots: A Door Way to Nanoscale Physics*, 1 edn, Springer. 5.1

Katsaros, G., Costantini, G., Stoffel, M., Esteban, R., Bittner, A. M., Rastelli, A., Denker, U., Schmidt, O. G. and Kern, K. (2005), 'Kinetic origin of island intermixing during the growth of Ge on Si(001)', *Physical Review B* **72**(19), 6. 5.1, 5.3

Kratzer, P., Liu, Q. K. K., Acosta-Diaz, P., Manzano, C., Costantini, G., Songmuang, R., Rastelli, A., Schmidt, O. G. and Kern, K. (2006), 'Shape transition during epitaxial growth of InAs quantum dots on GaAs(001): Theory and experiment', *Physical Review B* **73**(20), 8. 5.1, 5.5, 5.6

Landau, L. M. and Lifshitz, E. M. (1986), *Theory of Elasticity*, 3 edn, Pergamon Press. 2.4, 2.5.1, 3.3, 4.2.1, 4.4

Lang, C., Cockayne, D. J. H. and Nguyen-Manh, D. (2005), 'Alloyed Ge(Si)/Si(001) islands: The composition profile and the shape transformation', *Physical Review B* **72**(15), 9. 5.1

Leite, M. S., Medeiros-Ribeiro, G., Kamins, T. I. and Williams, R. S. (2007), 'Alloying mechanisms for epitaxial nanocrystals', *Physical Review Letters* **98**(16), 4. (document), 5.2, 5.1, 1, 5.1, 5.3

Leonard, F. and Tersoff, J. (2003), 'Competing step instabilities at surfaces under stress', *Applied Physics Letters* **83**(1), 72–74. 2.6.1

Li, A., Liu, F. and Lagally, M. G. (2000), 'Equilibrium shape of two-dimensional islands under stress', *Physical Review Letters* **85**(9), 1922–1925. (document), 2.1, 1, 3.1, 3.4, 4.1, 4.3

Li, Z., Singh, M. K., Toh, E. S., Tan, J. P. Y., Kin, M. and Foo, Y. L. (2007), 'Kinetically constraint zero- and one-dimensional heteroepitaxial island growth', *Applied Physics Letters* **90**(10), 3. 1, 4.1, 4.1, 4.3

Liao, X. Z., Zou, J., Cockayne, D. J. H., Jiang, Z. M., Wang, X. and Leo, R. (2000), 'Composition and its impact on shape evolution in dislocated Ge(Si)/Si islands', *Applied Physics Letters* **77**(9), 1304–1306. 6.2.2

Lim, D. K., Lee, D., Lee, H., Bae, S. S., Choi, J., Kim, S., Ji, C. X., Ragan, R., Ohlberg, D. A. A., Chang, Y. A. and Williams, R. S. (2007), 'Structure and electronic properties of self-assembled Pt silicide nanowires on Si(100)', *Nanotechnology* **18**(9), 4. 1, 4.1, 4.1, 4.3

Liu, N., Tersoff, J., Baklenov, O., Holmes, A. L. and Shih, C. K. (2000), 'Nonuniform composition profile in $In_{0.5}Ga_{0.5}As$ alloy quantum dots', *Physical Review Letters* **84**(2), 334–337. 5.1

Lu, W. and Suo, Z. (2001), 'Dynamics of nanoscale pattern formation of an epitaxial monolayer', *Journal of the Mechanics and Physics of Solids* **49**(9), 1937–1950. 2.5.1, 4.2.1

Malachias, A., Kycia, S., Medeiros-Ribeiro, G., Magalhaes-Paniago, R., Kamins, T. I. and Williams, R. S. (2003), '3D composition of epitaxial nanocrystals by anomalous

x-ray diffraction: Observation of a Si-rich core in Ge domes on Si(100)', *Physical Review Letters* **91**(17), 4. (document), 5.2, 5.1, 1, 5.1, 5.3

Medeiros-Ribeiro, G. and Williams, R. S. (2007), 'Thermodynamics of coherently-strained GexSi1-x nanocrystals on Si(001): Alloy composition and island formation', *Nano Letters* **7**(2), 223–226. 5.1, 1

Medeiros-Ribeiro, G., Bratkovski, A. M., Kamins, T. I., Ohlberg, D. A. A. and Williams, R. S. (1998), 'Shape transition of germanium nanocrystals on a silicon (001) surface from pyramids to domes', *Science* **279**(5349), 353–355. (document), 1.1, 1, 5.1, 5.1, 5.5, 5.6

Medhekar, N. V., Shenoy, V. B., Hannon, J. B. and Tromp, R. M. (2007*a*), 'Metastability in 2D self-assembling systems', *Physical Review Letters* **99**(15), 4. 3.5, 4.3

Medhekar, N. V., Shenoy, V. B., Hannon, J. B. and Tromp, R. M. (2007*b*), 'Self-assembling surface stress domains far from equilibrium', *Applied Physics Letters* **91**(25), 3. (document), 3.6, 4.1

Merdzhanova, T., Kiravittaya, S., Rastelli, A., Stoffel, M., Denker, U. and Schmidt, O. G. (2006), 'Dendrochronology of strain-relaxed islands', *Physical Review Letters* **96**(22), 4. 6.2.2

Moore, G. E. (1965), 'Cramming more components onto integrated circuits', *Electronics*. 1

Mullins, W. W. and Sekerka, R. F. (1963), 'Morphological stability of a particle growing by diffusion or heat flow', *Journal of Applied Physics* **34**(2), 323–329. 2.6.1, 4.3, 4.4

Owen, J. H. G., Miki, K. and Bowler, D. R. (2006), 'Self-assembled nanowires on

semiconductor surfaces', *Journal of Materials Science* **41**(14), 4568–4603. 1, 4.1, 5.7

Pimpinelli, A. and Villain, J. (1998), *Physics of crystal growth*, 1 edn, Cambridge University Press. 1

Plass, R., Bartelt, N. C. and Kellogg, G. L. (2002), 'Dynamic observations of nanoscale self-assembly on solid surfaces', *Journal of Physics-Condensed Matter* **14**(16), 4227–4240. 3.5

Plass, R., Last, J. A., Bartelt, N. C. and Kellogg, G. L. (2001), 'Nanostructures - Self-assembled domain patterns', *Nature* **412**(6850), 875–875. 1, 2.1, 4.1

Pohl, K., Bartelt, M. C., Figuera, J. d. l., Bartelt, N. C., Hrbek, J. and Hwang, R. Q. (1999), 'Identifying the forces responsible for self-organization of nanostructures at crystal surfaces', *Nature* **397**(6716), 238–241. 1

Pradhan, A., Ma, N. Y. and Liu, F. (2004), 'Theory of equilibrium shape of an anisotropically strained island: Thermodynamic limits for growth of nanowires', *Physical Review B* **70**(19), 4. 4.1, 4.3

Ross, F. M., Tromp, R. M. and Reuter, M. C. (1999), 'Transition states between pyramids and domes during Ge/Si island growth', *Science* **286**(5446), 1931–1934. 1, 4.1, 5.1, 5.5, 5.6

Schittkowski, K. (1986), 'NLPQL: A fortran subroutine solving constrained nonlinear programming problems', *Annals of Operations Research* **5**(2), 485–500. 2.4, 3.3, 5.2

Seul, M. and Andelman, D. (1995), 'DOMAIN SHAPES AND PATTERNS - THE PHENOMENOLOGY OF MODULATED PHASES', *Science* **267**(5197), 476–483. 1, 2.1, 4.1

Sheng, W. D. and Leburton, J. P. (2001), 'Electron-hole alignment in InAs/GaAs self-assembled quantum dots: Effects of chemical composition and dot shape', *Physical Review B* **63**(16), 4. 5.1

Shenoy, V. B., Kukta, R. V. and Phillips, R. (2000), 'Mesoscopic analysis of the structure and strength of dislocation junctions in fcc metals', *Physical Review Letters* **84**(7), 1491–1494. 6.2.2

Shumway, J., Williamson, A. J., Zunger, A., Passaseo, A., DeGiorgi, M., Cingolani, R., Catalano, M. and Crozier, P. (2001), 'Electronic structure consequences of In/Ga composition variations in self-assembled $In_xGa_{1-x}As$/GaAs alloy quantum dots', *Physical Review B* **6412**(12), 12. 5.1

Silverman, J. P. (1998), 'Challenges and progress in X-ray lithography', *Journal of Vacuum Science and Technology B* **16**(6), 3137–3141. 1

Singh, R., Harame, D. L. and Meyerson, B. S. (2005), 'Silicon-Germanium – Adnaced technology, modeling and design', *Proceedings of IEEE* **93**(9), 1519–1521. 1, 6.2.1

Sone, H., Mishima, T., Miyachi, A., Fukuda, T. and Hosaka, S. (2007), 'Growth control of self-assembled ErSi2 nanowires on Si(001) and Si(110) surfaces', *Microelectronic Engineering* **84**(5-8), 1491–1495. 1, 4.1, 4.1, 4.3

Sormunen, J., Riikonen, J., Mattila, M., Tiilikainen, J., Sopanen, M. and Lipsanen, H. (2005), 'Transformation of self-assembled InAs/InP quantum dots into quantum rings without capping', *Nano Letters* **5**(8), 1541–1543. 5.7

Spencer, B. J. and Blanariu, M. (2005), 'Shape and composition map of a prepyramid quantum dot', *Physical Review Letters* **95**(20), 4. (document), 5.1, 5.1, 5.6

Stangl, J., Holy, V. and Bauer, G. (2004), 'Structural properties of self-organized semiconductor nanostructures', *Reviews of Modern Physics* **76**(3), 725–783. 1, 5.1

Sunamura, H., Usami, N., Shiraki, Y. and Fukatsu, S. (1996), 'Observation of lateral confinement effect in Ge quantum wires self-aligned at step edges on Si(100)', *Applied Physics Letters* **68**(13), 1847–1849. 1, 4.1

Takayanagi, K., Tanishiro, Y., Takahashi, S. and Takahashi, M. (1985), 'Structure-analysis of SI(111)-7×7 reconstructed surface by transmission electron-diffraction', *Surface Science* **164**(2-3), 367–392. 2.2

Tersoff, J. and Tromp, R. M. (1993), 'Shape transition in growth of strained islands - spontaneous formation of quantum wires', *Physical Review Letters* **70**(18), 2782–2785. 2.1, 1, 3.1, 3.4, 4.1, 4.3

Thayer, G. E., Hannon, J. B. and Tromp, R. M. (2004), 'Shape and stability of self-assembled surface domains', *Nature Materials* **3**(2), 95–98. (document), 2.1, 2.4, 2.3, 2.4, 2, 3.2, 3.3

Tromp, R. M. and Reuter, M. C. (1991), 'Design of a new photoemission/low-energy electron microscope for surface studies', *Ultramicroscopy* **36**(1-3), 99–106. 2.3

Twesten, R. D. and Gibson, J. M. (1994), 'Measurement of Si(111) surface stress by a microscopic technique', *Physical Review B* **50**(23), 17628–17631. 2.2, 2.4, 2.5.2

Vailionis, A., Cho, B., Glass, G., Desjardins, P., Cahill, D. G. and Greene, J. E. (2000), 'Pathway for the strain-driven two-dimensional to three-dimensional transition during growth of Ge on Si(001)', *Physical Review Letters* **85**(17), 3672–3675. 5.1, 5.5, 5.6

van Gastel, R., Bartelt, N. C. and Kellogg, G. L. (2006), 'Reversible shape transition of Pb islands on Cu(111)', *Physical Review Letters* **96**(3), 4. 2.1, 1

Wang, Z. M. (2007), *Self-Assembled Quantum Dots (Lecture Notes in Nanoscale Science and Technology)*, 1 edn, Springer. 5.1

Whitesides, G. M. and Grzybowski, B. (2002), 'Self-assembly at all scales', *Science* **295**(5564), 2418–2421. 1, 4.1

Williams, E. D. and Bartelt, N. C. (1991), 'Thermodynamics of surface morphology', *Science* **251**(4992), 393–400. 2.6.1

Williams, R. S. (2007), 'The evolution of technology for electronic materials over the last 50 years', *Journal of the Minerals, Metals and Materials Society* **59**(2), 58–65. 1

Wulff, G. (1901), 'Zur frage der geschwindigkeit des wachstums und der auflösung der krystallflagen', *Zeitschrift für krystallographie und mineralogie* **34**, 449. 2.6.1, 2.6.1, 3.1

You, J. P., Choi, J. H., Kim, S., Li, X. M., Williams, R. S. and Ragan, R. (2006), 'Regular arrays of monodisperse platinum/erbium disilicide core-shell nanowires and nanoparticles on Si(001) via a self-assembled template', *Nano Letters* **6**(9), 1858–1862. 1, 4.1, 4.1, 4.3

Zandvliet, H. J. W. (2000), 'Energetics of Si(001)', *Reviews of Modern Physics* **72**(2), 593. (document), 4.5, 4.4, 4.4

Zhu, J. Z., Chen, L. Q., Shen, J. and Tikare, V. (1999), 'Coarsening kinetics from a variable-mobility Cahn-Hilliard equation: Application of a semi-implicit Fourier spectral method', *Physical Review E* **60**(4), 3564–3572. 2.5.1, 4.2.1

Zielasek, V., Liu, F., Zhao, Y. G., Maxson, J. B. and Lagally, M. G. (2001), 'Surface stress-induced island shape transition in Si(001) homoepitaxy', *Physical Review B* **6420**(20), 4. 2, 4.4, 4.4, 4.4